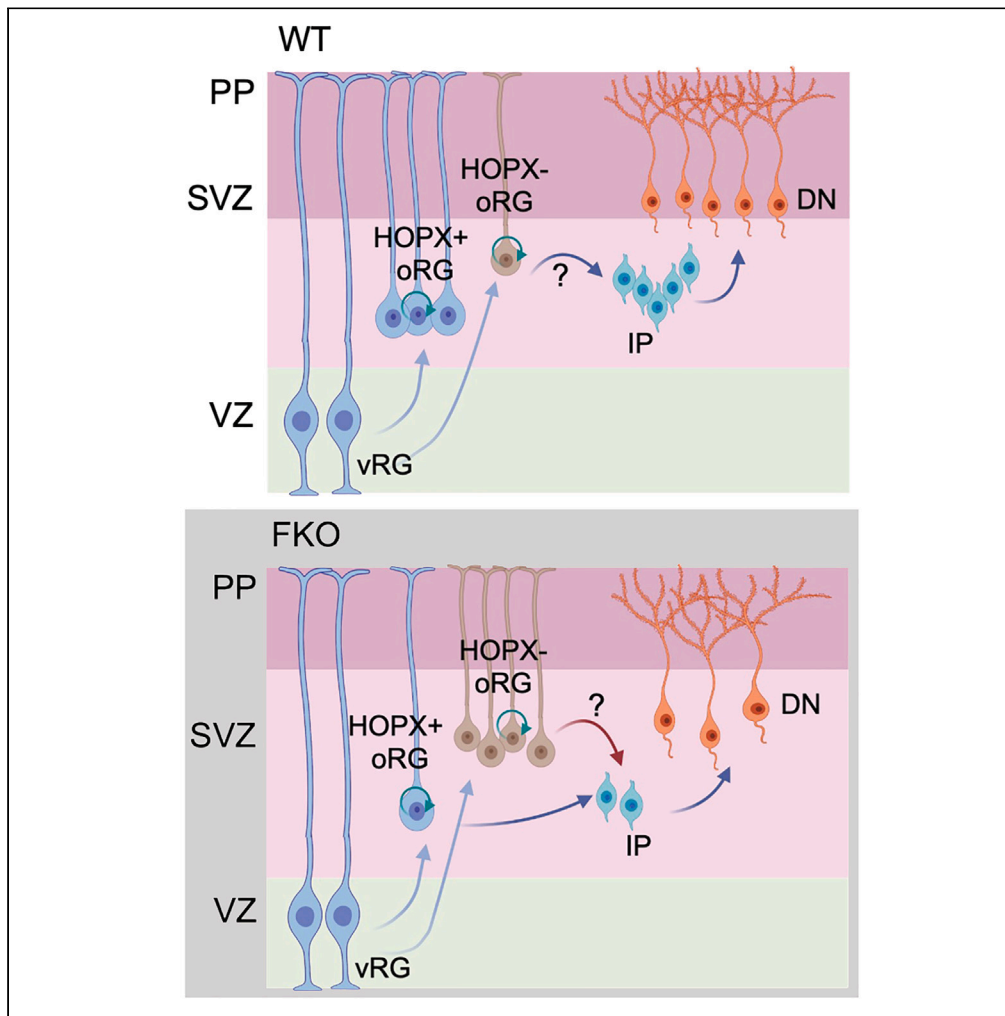# iScience

Article

FEZ1 participates in human embryonic brain development by modulating neuronal progenitor subpopulation specification and migrations

Yinghua Qu, Jonathan Jun-Yong Lim, Omer An, Henry Yang, Yi-Chin Toh, John Jia En Chua

yichin.toh@qut.edu.au (Y.-C.T.)
phsjcje@nus.edu.sg (J.J.E.C.)

Highlights

FEZ1 expression is turned on early during human brain development

Deletion of FEZ1 causes expansion of HOPX⁻ outer radial glial cells

Ectopic localization of neuroprogenitors occurs in the absence of FEZ1

Cortical layer formation is disrupted in the absence of FEZ1

Article

FEZ1 participates in human embryonic brain development by modulating neuronal progenitor subpopulation specification and migrations

Yinghua Qu,[1,2] Jonathan Jun-Yong Lim,[1,6,7] Omer An,[3] Henry Yang,[3] Yi-Chin Toh,[2,4,5,*] and John Jia En Chua[1,6,7,8,9,*]

SUMMARY

Mutations in the human fasciculation and elongation protein zeta 1 (*FEZ1)* gene are found in schizophrenia and Jacobsen syndrome patients. Here, using human cerebral organoids (hCOs), we show that *FEZ1* expression is turned on early during brain development and is detectable in both neuroprogenitor subtypes and immature neurons. FEZ1 deletion disrupts expression of neuronal and synaptic development genes. Using single-cell RNA sequencing, we detected abnormal expansion of homeodomain-only protein homeobox (HOPX)⁻ outer radial glia (oRG), concurrent with a reduction of HOPX⁺ oRG, in FEZ1-null hCOs. HOPX⁻ oRGs show higher cell mobility as compared to HOPX⁺ oRGs. Ectopic localization of neuroprogenitors to the outer layer is seen in FEZ1-null hCOs. Anomalous encroachment of TBR2⁺ intermediate progenitors into CTIP2⁺ deep layer neurons further indicated abnormalities in cortical layer formation these hCOs. Collectively, our findings highlight the involvement of FEZ1 in early cortical brain development and how it contributes to neurodevelopmental disorders.

INTRODUCTION

Cortical development is a multistage process involving neurogenesis, cell migration, differentiation, and maturation that occurs over an extended time frame.[1–4] Despite a wealth of knowledge in the identities of transcription factors driving neurogenesis and differentiation of neural progenitors to different neuronal subtypes, the compendium of other genes participating the various developmental stages is only beginning to be progressively unraveled. Significantly, mutations in a number of them have been associated with human brain disorders with neurodevelopmental origins, including neuropsychiatric disorders such as schizophrenia (SCZ), attention-deficit/hyperactivity disorder (ADHD), and autism spectrum disorders (ASD).[5–7] Nevertheless, how such genes contribute to these disorders remain incompletely understood.

One such implicated gene is fasciculation elongation protein zeta 1 (FEZ1). Its invertebrate homolog, *Unc-76,* was initially identified as necessary for nervous system development in *Caenorhabditis elegans. unc-76* mutants showed axonal outgrowth and fasciculation defects as well as abnormalities in synapse formation and organization.[8–11] These phenotypes were also recapitulated in *Drosophila unc-76* mutants.[12,13] Importantly, deletion of FEZ1 in mammalian neurons severely retarded outgrowth and branching of axons and dendrites, suggesting that impaired neurodevelopment as a result of FEZ1 loss can contribute to neurodevelopment and neuropsychiatric disorders.[14–16] Supporting this notion, FEZ1-knockout mice exhibited behavioral defects akin to those observed in SCZ and ADHD patients.[17,18]

Significantly, the FEZ1 gene is also frequently lost in Jacobsen syndrome patients, a rare disorder affecting children where the terminal region of chromosome 11q is deleted.[19–21] These patients are frequently diagnosed with ADHD, while ASD, SCZ, and, rarely, bipolar disorders have also been documented. Furthermore, *FEZ1* polymorphisms and changes in brain expression of *FEZ1* have been detected in a cohort of SCZ patients.[15,22–26] These observations point toward *FEZ1*'s importance in human brain development and its dysfunction as contributing to these disorders. However, its roles in human cortical brain development and its involvement in neurodevelopmental disorders have not been formally established.

[1]Department of Physiology, Yong Loo Lin School of Medicine, National University of Singapore, Singapore 117456, Singapore
[2]Department of Biomedical Engineering, National University of Singapore, Singapore 117583, Singapore
[3]Cancer Science Institute of Singapore, National University of Singapore, Singapore 117599, Singapore
[4]School of Mechanical, Medical and Process Engineering, Queensland University of Technology, Brisbane, QLD 4059, Australia
[5]Centre for Biomedical Technologies, Queensland University of Technology, Brisbane, QLD 4059, Australia
[6]Healthy Longevity Translational Research Program, Yong Loo Lin School of Medicine, National University of Singapore, Singapore 117456, Singapore
[7]LSI Neurobiology Programme, National University of Singapore, Singapore 117456, Singapore
[8]Institute for Molecular and Cell Biology, A*STAR, Singapore 138473, Singapore
[9]Lead contact
*Correspondence: yichin.toh@qut.edu.au (Y.-C.T.), phsjcje@nus.edu.sg (J.J.E.C.)
https://doi.org/10.1016/j.isci.2023.108497

Here, using human cerebral organoids (hCO) as a human brain development model, we observed that *FEZ1* mRNA and protein, which was absent in human embryonic stem cells (hESCs), became detectable in neuroprogenitor cell types early during hCO development and continued to increase as the organoids matured. While loss of FEZ1, engineered by CRISPR-Cas9 gene editing, did not cause significant morphological changes in FEZ1-null hCOs, RNA-seq analyses uncovered a substantial number of differentially expressed genes enriched in neuronal development as well as synaptic function, supporting previous studies demonstrating its importance in these biological processes. scRNA-seq analyses of hCOs further uncovered an abnormal expansion of homeodomain-only protein homeobox negative (HOPX⁻) outer radial glial (oRG) in FEZ1-null hCOs that came at the expense of a diminished pool of HOPX⁺ canonical oRG. Analyses of differentially expressed genes (DEGs) between HOPX⁻ oRG and HOPX⁺ oRG indicated differences in expression of genes involved in actin dynamics. Supporting this, oRGs in FEZ1-null hCOs showed higher globular (G-) to filamentous (F-) actin ratios and anomalous cell migration *in situ*. These changes were accompanied by a corresponding increase and anomalous expansion of TBR2⁺ intermediate progenitors (IP) into a reduced CTIP2⁺ layer of deep layer neurons in FEZ1-null hCOs, resulting in early cortical lamination abnormalities. Taken together, our results supported earlier findings of FEZ1's roles in neuronal development and synapse formation and additionally uncovered an unexpected involvement of FEZ1 in influencing developmental trajectories and cortical layer formation during cortical brain development.

RESULTS

Expression of FEZ1 begins early during human brain development

FEZ1 deletion has been identified in Jacobsen syndrome patients, a rare human neurodevelopmental disorder.[21,27,28] However, its role in human brain development is unknown. In rodents, detection of *FEZ1* mRNA and protein coincided with the height of neurogenesis, indicating its likely involvement in the earliest phases of brain development.[17,29] To examine whether this might occur during human brain development, we generated hCOs following a non-patterning factor-based protocol.[30] As reported, rosette-like structures with apical ventricular-like zones (VZ-like) surrounded by PAX6⁺ cells, indicating neuroepithelial cells (NE), or radial glia (RG), appeared in developing hCOs as early as day 10 (D10) (Figure S1A).[30,31] At D28, sequential layering of TBR2⁺ intermediate progenitors (IP) and CTIP2⁺ deep layer neurons were observed, indicating that cortical layering has begun at this time, which concurred with earlier reports (Figure S1B).[31,32] Staining with PAX6, TBR2, and CTIP2 were used to delineate VZ-like, subventricular-like zones (SVZ-like), and preplate-like (PP-like) regions, respectively.[30,31,33,34]

Consistent with the early expression of FEZ1 in rodent brain development, FEZ1 expression was apparent as cytosolic puncta within PAX6⁺ neuroepithelial cells at VZ-like regions of D10 hCOs (Figure 1A). By D28, both FEZ1 levels and the proportion of PAX6⁺ cells expressing FEZ1 had further increased across the rosette-like structure. By D60, FEZ1 puncta could be observed in newly derived TUJ1⁺ neurons in the cortical plate (CP)[31,35] (Figure 1A). Immunoblot and real-time PCR analyses further confirmed that FEZ1 expression, while virtually undetectable in undifferentiated hESCs, progressively increased as hCOs developed (Figures 1B and 1C). To further ascertain that FEZ1 expression was switched on at the earliest stages of cortical development, we directly derived human neuroepithelial cells (hNEs) from hESCs.[36] As observed in hCOs, increased levels of both *FEZ1* mRNA and protein followed differentiation of hESCs (Figures 1D and 1E) and human induced pluripotent stem cells (hiPSCs) to hNE (Figure S1C). Taken together, our results indicated that FEZ1 expression began at the early stages of neural specification independently of the induction protocol or culture configuration, supporting its involvement in early human brain development.

Loss of FEZ1 alters expression of genes involved in early brain and neuronal development

To examine the role of FEZ1 in early human brain development, we generated FEZ1-null hESCs using a lentivirus-mediated CRISPR-Cas9 strategy that targeted exon 2 of the *FEZ1* gene (Figure 2A).[14,16] Following puromycin selection, 24 distinct clones were independently picked up for expansion. All clones were subjected to PCR amplification and sequencing of the sgRNA target region. Three of these clones contained homozygous mutations with an identical insertion of an adenine residue at position 366 of the coding region in the mRNA sequence (Figure S2). This introduced a frameshift in the open reading frame of the coding region, giving rise to a prematurely truncated peptide containing the first 58 amino acids of FEZ1, followed by the addition of 6 non-templated amino acids (Figure 2A).

Separately, we also generated FEZ1-null clones using hiPSC lines using the same CRISPR strategy. Four out of 24 distinct and independently selected clones were found to contain indel mutation at the target site. Three of these clones contained the identical frameshift insertion found in the FEZ1-null hESC clones (Figure 2A). The last clone (iC21) contained 10 nucleotide deletion followed by a single base pair in-frame insertion within the coding region (position 356–375). This resulted in the predicted translation of a full-length FEZ1 missing 3 amino acids at positions 56–58 and the substitution of methionine at position 59 with leucine. Since most of the N- and C-terminal functional motifs were preserved, iC21 was not further studied.

Of the FEZ1-null clones, one hESC clone (KO hESC_C5) and one hiPSC clone (KO hiPSC_iC4) were selected for further study. Immunoblot analyses of lysates from hNEs and hCOs generated from these 2 independent clones confirmed the successful elimination of FEZ1 expression (Figures 2B and S3A). KO hESC_C5 (henceforth called FEZ1-null hESC) was used as the representative FEZ1-null H1 hESC clone in all subsequent studies since all FEZ1-null hESC and iPSC clones possessed identical frameshift insertion site in *FEZ1* gene. We further determined the absence of gross chromosomal abnormalities in this clone after gene editing by karyotyping (Figure S3B). Although there was a significant increase in the cell proliferation rate of FEZ1-null hESC at day 4 of *in vitro* culture (Figure S3C), the expression of the pluripotency markers SOX2, LIN28, NANOG, and SSEA4 were unaffected in WT and FEZ1-null hESCs (Figure S3D). This indicated that loss of FEZ1 did not cause adverse effects on stem cell pluripotency or survival.

Macroscopically, loss of FEZ1 did not appear to affect generation of hCOs from the FEZ1-null hESC. There were no significant differences in gross morphology or size of hCOs derived from wild type (WT) and FEZ-null hESCs over a culture period of 120 days (Figure 2C). Moreover,
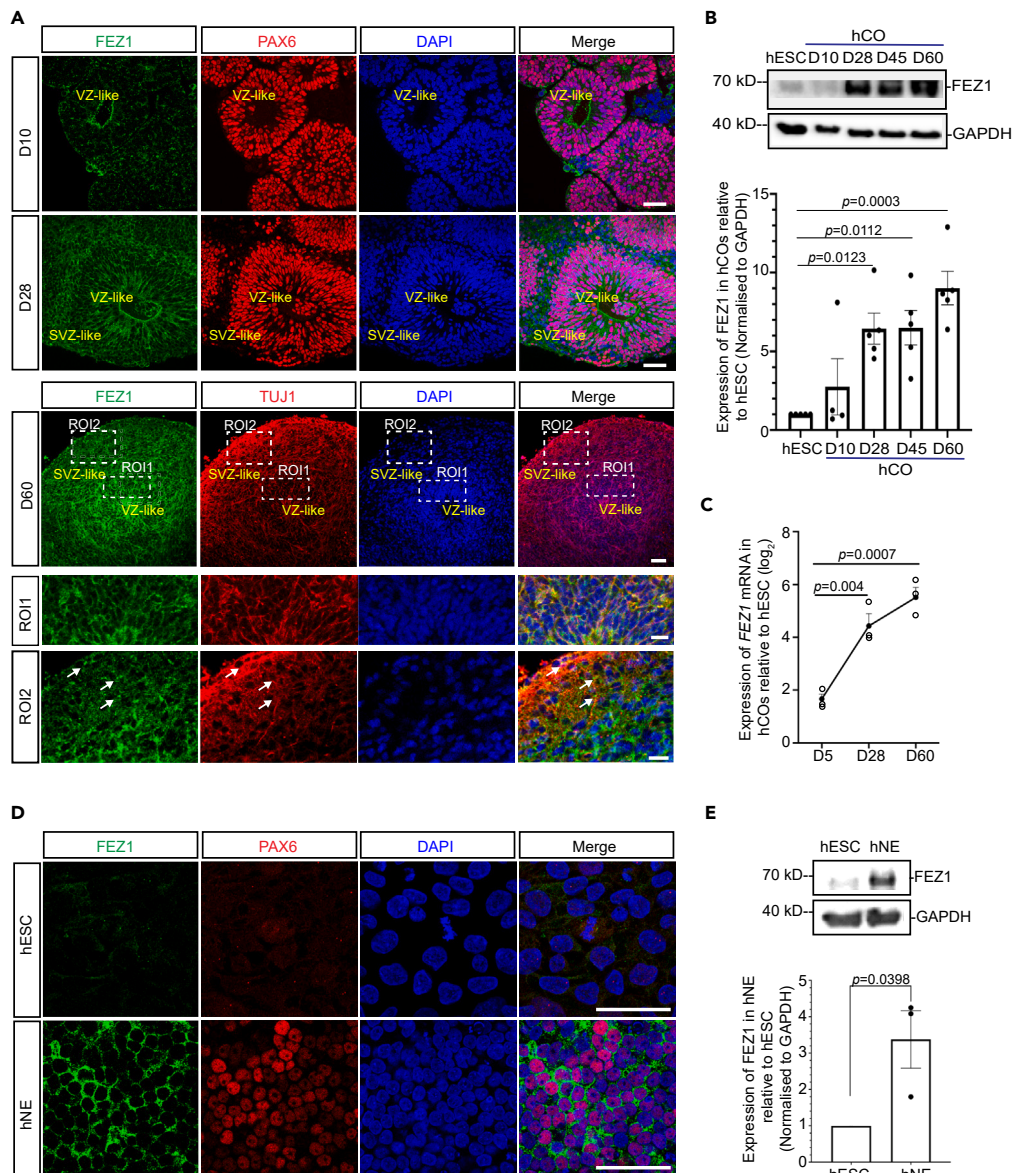
Figure 1. FEZ1 expression increased progressively during human cerebral organoid (hCO) development

(A) Immunofluorescence (IF) staining of FEZ1 with the hNE marker PAX6 in D10 and D28 hCOs (upper panel), co-staining of FEZ1 with the neuronal marker TUJ1 in D60 hCOs (lower panel). Region of interests (ROIs) shows higher magnification of the ventricular-like zone (VZ-like) and subventricular-like zone (SVZ-like) regions in D60 hCOs. Punctate FEZ1 staining is visible. In ROI2, arrows indicate FEZ1 puncta along TUJ1$^+$ neurites in the SVZ-like region. Scale bars, 50 μm (ROI1) and 20 μm (ROI2).

(B) Immunoblot and quantification of FEZ1 protein expression during hCO development. Values represent mean ± SEM (n = 5 independent organoid differentiations and at least 2 organoids for WT and FEZ1-null, respectively. Ordinary one-way ANOVA with Tukey's multiple comparisons test with p values indicated).

(C) RT-qPCR analysis of FEZ1 mRNA expression in D5 to D60 hCOs. Results were normalized against GAPDH and expressed relative to FEZ1 levels in undifferentiated human embryonic stem cells (hESCs). Values represent mean ± SEM (n = 3 independent organoid differentiations and at least 2 organoids for WT and FEZ1-null, respectively. Ordinary one-way ANOVA with Tukey's multiple comparisons test with p values indicated).

(D) IF staining of FEZ1 in hESC and hNE shows that FEZ1 expression is switched on upon differentiation of hESC to human neuroepithelium (hNE). Scale bars, 50 μm.

(E) Immunoblot and quantification of FEZ1 protein expression in hESC (H1) and hNE. Values represent mean ± SEM (n = 3 independent hESC to hNE differentiations, unpaired t test determined the two-tailed p value as indicated). VZ-like: ventricular-like zone; SVZ-like: subventricular-like zone.

Figure 2. Deletion of FEZ1 altered expression of genes involved in neurodevelopment and neurodevelopmental disorders

(A) CRISPR-Cas9-mediated FEZ1 deletion in hESCs and hiPSCs. All clones selected from both hESC (H1) and hiPSC lines consistently harbored a 1 bp insertion (shown in red) in exon 2. Only one hiPSC clone (iC21) contained a 9 bp deletion (shown in magenta).

(B) Immunoblot of FEZ1 expression in hNE and developing hCOs confirmed the successful ablation of FEZ1 expression in FEZ1-null hESC_C5 clone.

(C) hCOs generated from wild type (WT) hESC H1 line and FEZ1-null hESC_C5 clone showed no gross differences in morphology and size over 120-day culture period. Scale bar: 500 μm. Values represent mean ± SEM (n = 4 independent organoid differentiations and at least 14 organoids for WT and FEZ1-null, respectively. Each data points represent measured diameter of one organoid. At least 4 WT and FEZ1-null organoids per biological repeat were measured. Analyses were performed using two-way ANOVA with Šidák's multiple comparisons (ns: not statistically significant).

(D) Venn diagram (top panel) and volcano plot (bottom panel) of significant differentially expressed genes (DEGs) ($log_2FC > 1$ or < -1; adjusted p value < 0.05) between D10 FEZ1-null hCO and D10 WT hCOs. Top 25 DEGs are shown in the plot. (n = 4 independent organoid differentiations with 40 organoids for WT and FEZ1-null, respectively.) (E) Gene ontology (GO) analysis of significant DEGs in D10 FEZ1-null hCOs using Metascape (https://metascape.org/gp/index.html#/main/step1). Statistical significances of enriched GO terms are shown in the color-coded legend.

(F) Disease enrichment analysis of significant DEGs in D10 FEZ1-null hCOs using Enricher (https://maayanlab.cloud/Enrichr/). DEGs in FEZ1-null hCOs were significantly associated with neurodevelopment and neurodegeneration disorders.

immunofluorescent staining of both groups of hCOs at D10 with PAX6 and Nestin shows the formation of rosette-like structures, lined by PAX6⁺ neuroprogenitor cells (Figure S3E). Supporting these observations, hCOs derived from the independently generated hiPSC FEZ1-null clone (KO hiPSC_iC4) also showed no difference in size in comparison to their WT hiPSC counterparts, although a small decrease in size of the mutant organoids was seen from D45 (Figure S3F).

Although deletion of *FEZ1* gene did not induce gross aberrations in hCO formation and morphology, it could still cause changes to cellular signaling and programming pathways. Indeed, bulk RNA-seq analyses of WT and FEZ1-null hCOs at D10 uncovered significant changes between the 2 transcriptomes. In total, 425 differentially expressed genes (DEGs) were identified (Figure 2D; Table S1). Of these, 42 genes were upregulated, and 383 genes were downregulated in FEZ1-null as compared to WT hCOs (Figure 2D). Gene ontology (GO) enrichment analysis revealed that genes involved in neuron projection development and synaptic transmission were significantly over-represented in the down-regulated genes (Figure 2E, upper panel; Table S2). These results correlated well with the established function of FEZ1 in neuronal development and synaptic function.[9,14–16,37] Genes upregulated in the absence of FEZ1 were primarily associated with Wnt signaling and sensory system development (Figure 2E, bottom panel; Table S3). Wnt signaling pathways is implicated in early brain development and FEZ1 is a known target of Wnt/β-catenin signaling.[38,39]

Notably, DEGs in FEZ1-null hCOs were significantly enriched for genes associated with neurodevelopment and neurodegenerative disorders (Figure 2F). FEZ1 abnormalities have been previously linked to Alzheimer's and Parkinson's disease as well as ADHD and SCZ-like behavior in FEZ1 knockout mice and in Jacobsen syndrome (JS) patients.[9,17,18,21,40] Additionally, genes associated with depression and intellectual disability were highly represented in FEZ1-null hCOs. Collectively, these results indicated FEZ1's involvement in early human brain development and that loss of FEZ1 potentially triggers changes in biological pathways contributing to neurodevelopmental as well as neurodegenerative disorders.

FEZ1-null hCOs contain a disproportionately larger population of HOPX⁻ oRG

Changes in expression of genes regulating neuronal differentiation were observed in FEZ1-null hCOs (Figure 2E). This suggested *FEZ1* deletion may trigger alterations in developmental trajectories of neural progenitors. We performed single-cell RNA-seq (scRNA-seq) to interrogate for changes in sub-populations of cells in D28 hCOs when cortical lamination had already started (Figure S1B).[31,32,41] A total of 7800 and 9254 cells were analyzed from five WT and five FEZ1-null hCOs, respectively. Neural progenitors and neurons were identified and grouped according to known markers as previously reported (Figures 3A and S4A; Table S4).[33,42,43] In total, 14 unique cell clusters could be identified, corresponding to ventricular neuroepithelium/radial glia cells (vNE/vRG: *LIX1, NES, HMGA2, PAX6*); dividing vNE/vRG (*MKI67, LIX1, PAX6, ASPM*); truncated radial glia cells (tRG: *CRYAB, EGR1, HMGA2*; HOPX⁺ outer radial glia cells (HOPX⁺ oRG: *HOPX, BMP7, CLU, FEZF2*); HOPX⁻ outer radial glia cells (HOPX⁻ oRG: *FABP7, MOXD1, QKI*), which expressed oRG markers that are not represented in aforementioned HOPX⁺ oRG cluster[33,42–44]; dividing oRG (*MIK67, HJURP, FABP7, CLU, FEZF2, HOPX*); choroid plexus (CP: *TTR, OTX2*); intermediate progenitor cells (IP: *EOMES, DCX, BEUROG1*); dividing IP (*EOMES, MKI67, NEUROG1*); new born neurons (*STMN2, DCX*); deep layer neurons (*STMN2, NEUROD6, BCL11B*); upper layer neurons (*POU3F2, BHLHE22*); interneurons (*DLX5, GAD2, DLX1*); and pericytes (*COL3A1,LUM*). Among neurons and their progenitor cells, both the proportion of cells expressing *FEZ1* as well as the level of *FEZ1* mRNA increased as progenitor cells sequentially develop into deep and upper layer neurons in WT hCOs, which agreed with results obtained by immunostaining (Figures 1A and 3B).

Of the 14 unique cell clusters identified, changes in the proportion of HOPX⁻ oRG and HOPX⁺ oRG clusters were most apparent between FEZ1-null and WT hCOs (Figure 3C). The percentage of HOPX⁺ oRG was dramatically reduced from 78.59% in WT hCOs to 21.41% in FEZ1-null hCOs. In comparison to this, the population of HOPX⁻ oRG increased substantially from 11.8% in WT HCOs to 88.2% in FEZ1-null hCOs (Figure 3C). Both HOPX⁺ and HOPX⁻ oRG are present during cortical development, but their molecular signature remains incompletely defined.[44] The presence of both types of oRGs were further supported by correlative analysis of our bulk RNA-seq data against those obtained from human brain transcriptome[45] (Figure S4B). We noticed that *FEZ1* expression was higher in HOPX⁺ oRG as compared to HOPX⁻ oRG in the pooled oRG populations, suggesting that *FEZ1* expression is required for, or at least, accompanies the development of HOPX⁺ oRG (Figure S4C). Closer examination of markers expressed by both clusters further showed that HOPX⁺ oRGs also expressed

A

B
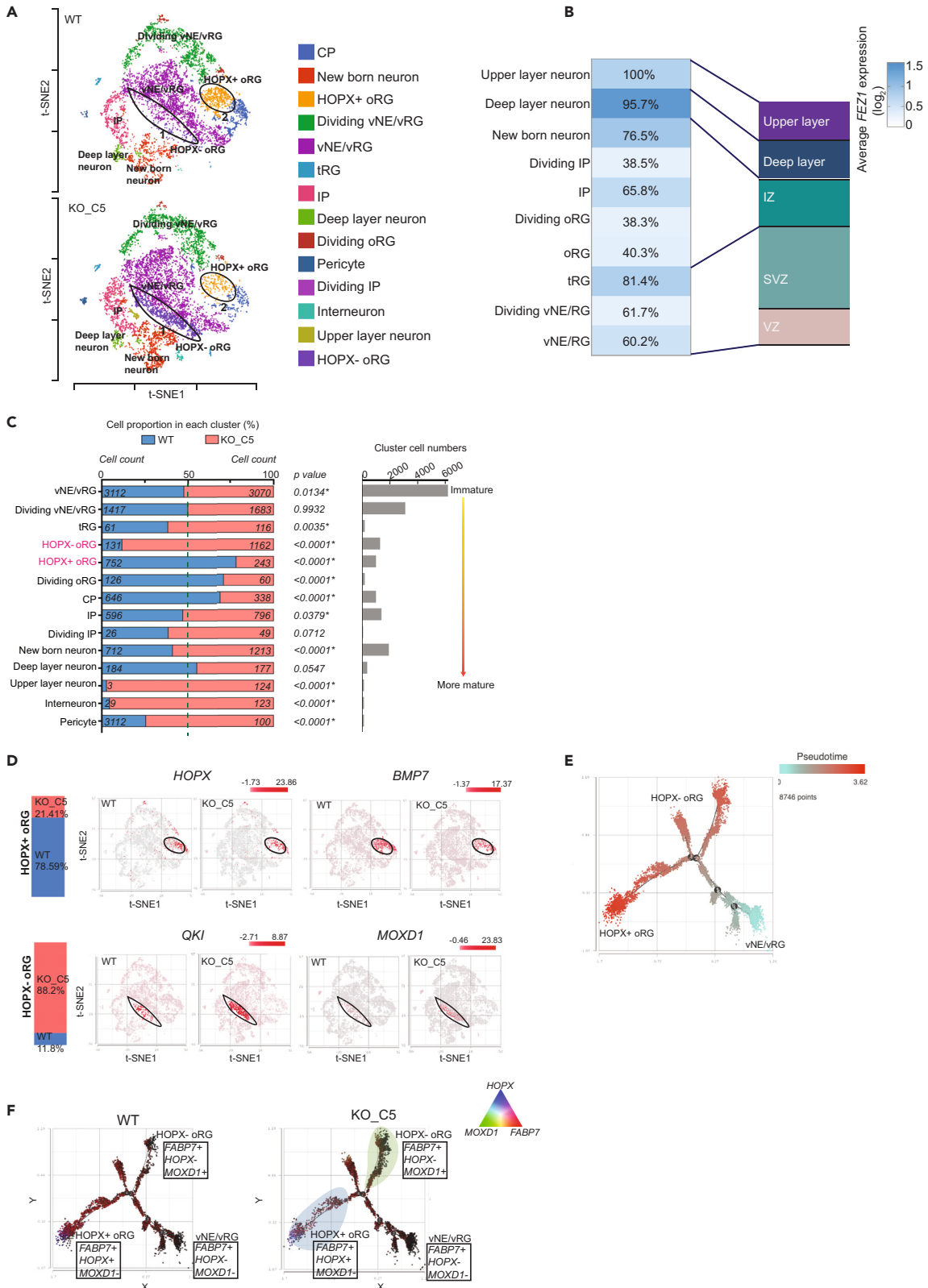

C

D

E

F

Figure 3. Single-cell RNA (scRNA) sequencing analyses uncovered alterations in development trajectories of outer radial glial (oRG) subpopulations in FEZ1-null hCOs

(A) t-SNE plots showing the distribution of various cell populations in D28 WT and FEZ1-null hCOs. Data were generated from five WT and FEZ1-null hCOs. Areas encircled with black ovals delineated HOPX⁺ oRG and HOPX⁻ oRG. vNE/vRG: ventricular neuroepithelium/radial glia cells; tRG: truncated radial glia cells; HOPX⁻ oRG: HOPX⁻ outer radial glia cells; HOPX⁺ oRG: HOPX⁺ outer radial glia cells; CP: choroid plexus; IP: intermediate progenitor.

(B) Relative expression levels of *FEZ1* mRNA in all classes of neuroprogenitor and newborn/immature neurons identified. Numbers in the boxes indicate percentages of cells expressing *FEZ1* in the corresponding cell clusters.

(C) Proportion of cells in each cell cluster in WT versus FEZ1-null hCOs. Cell clusters are arranged in progressing levels of differentiation, beginning from vNE/vRG to upper layer neurons. Interneuron and pericyte clusters are indicated at the bottom of the chart. Total cell numbers identified in each cell cluster are plotted on the right panel. Clusters belonging to HOPX⁺ oRG and HOPX⁻ oRG showed the largest changes between the 2 hCO groups. Statistical analysis was conducted and p *values* < 0.05 shows significant difference in cell numbers between WT and FEZ1-null hCO.

(D) t-SNE plots showing expression of *HOPX* and *BMP7* in HOPX⁺ oRG, and *QKI*, and *MOXD1* in HOPX⁻ oRG clusters of WT and FEZ1-null hCOs, respectively.

(E) Pseudotime analysis indicated that HOPX⁺ oRGs were in a more mature state as compared to HOPX⁻ oRGs.

(F) Trajectory inference analysis of three cell clusters (vNE/vRG, HOPX⁺ oRG, and HOPX⁻ oRG) indicated that both HOPX⁻ oRG and HOPX⁺ oRG originated from vNE/vRG. In FEZ1-null hCOs, changes in developmental trajectories led to an increase in the HOPX⁻ oRG (shaded in green) and a decrease in the HOPX⁺ oRG (shaded in blue). (E) and (F) were analyzed using Partek Flow.

BMP7, markers characteristic of classical oRGs (Figures 3D and S4A; Table S4).[33,42,43] In comparison to this, HOPX⁻ oRG did not express HOPX. Instead, they express *MOXD1*, *QKI*, and *CLU*, which are also expressed in vRG and early-stage oRG.[33,43,46,47] Supporting these observations, the pseudotime value of HOPX⁻ oRG lies intermediate between vNE/vRG and HOPX⁺ oRG, suggesting HOPX⁻ oRG were at a more immature or earlier stage of development as compared to HOPX⁺ oRG[48–50] (Figure 3E). Both oRG populations initially originated from vNE/vRG as revealed by developmental trajectory analyses, but they subsequently diverged to form 2 discrete clusters (Figures 3E and 3F). With loss of FEZ1, oRG developmental trajectory preferentially moved toward HOPX⁻ oRG expressing MOXD1 and QKI (Figure 3F). This suggests that the generation of cell types downstream of these neuroprogenitors could be affected, which may alter subsequent brain development.

Lamination abnormalities in FEZ1-null hCOs

In the primate brain, oRGs residing in SVZ are largely responsible for producing the diversity of cortical layer neurons during neocortex expansion.[33,51] The developmental trajectory of oRG is of particular interest in neurodevelopmental disorders as it is unique to human and primate brain development and largely absent in mouse brains.[52–54] Abnormalities associated with oRG subpopulation specification can contribute to cortical malformations that lead to alterations in neuronal connectivity.[55,56] A disproportionate increase in the number of HOPX⁻ oRG over classical HOPX⁺ oRG cells in FEZ1-null over WT hCOs is likely to alter subsequent generation of neuronal subtypes that would affect the eventual composition of cortical neurons as well as formation of cortical layers.[42,44,57,58]

To determine if cortical layer formation could be affected in the absence of FEZ1, D28 hCOs were stained for PAX6, TBR2 (IP), and CTIP2 (deep layer neurons) to mark the regions of VZ-like, SVZ-like, and PP-like regions, respectively.[30,31,33,34] Proper cortical lamination could be observed in WT hCOs, where VZ-like, SVZ-like, and PP-like layers were arranged concentrically from the center to the outermost layers (Figure 4A).[34,59] In comparison, there was conspicuous overlapping of the TBR2⁺ and CTIP2⁺ regions in FEZ1-null hCOs (Figure 4A). In particular, the distribution of TBR2⁺ cells can be observed to encroach into the CTIP2⁺ layer. This was accompanied by a slight but significant decrease in percentage of TBR2⁺ cells in the SVZ-like region (27.2% ± 2.2% FEZ1-null hCOs; 34.7% ± 1.7%, WT hCOs) and a corresponding increase in the PP-like region (28.9 ± 2.7% in FEZ1-null hCOs; 22% ± 1.6% in WT hCOs) (Figure 4B). Conversely, the percentage of CTIP2⁺ cells in the PP-like region was reduced in FEZ1-null hCOs (38.5% ± 2.5% in FEZ1-null hCOs; 52.9% ± 2.5% in WT hCOs), which was accompanied by an increase in the SVZ-like region (27.4% ± 1.8% in FEZ1-null hCOs; 16.3% ± 1.1% in WT hCOs) (Figure 4B). Defective lamination was also observed in hCOs generated from the FEZ1-null hiPSCs (Figure S5), supporting that loss of FEZ1 indeed led to lamination defects during early corticogenesis in FEZ1-null hCOs (Figure 4C).

Next, we examined if cortical layering abnormalities could be captured in our scRNA-seq dataset. Based on the quantification of cell populations via scRNA-seq, we observed most of the cell types have a significant change in cell numbers comparing between WT and FEZ1-null hCO. In particular, there was a slight decrease in the number of CTIP2⁺ deep layer neurons in FEZ1-null hCOs (49.03% in FEZ1-null hCOs; 50.97% in WT hCOs), and the pool of TBR2⁺ IPs was significantly expanded in FEZ1-null hCOs (57.18% in FEZ1-null hCOs; 42.82% in WT hCOs) (Figure 3C). Collectively, these results indicated that production of IP and the specification of cortical lamination, in particular of deep layer neurons are dysregulated in FEZ1-null hCOs.

HOPX⁻ oRG exhibit higher levels of actin dynamics

To gain further insight into how the shift toward HOPX⁻ oRG causes lamination defects, we examined which genes were differentially expressed in HOPX⁻ versus HOPX⁺ oRG cells. DEGs between the two populations of oRG were extracted from WT and FEZ1-null hCOs and visualized using the BBrowser (Venice algorithm [FDR<0.05]) (Figure 5A; Table S5).[60–62] Genes that were most significantly upregulated in the HOPX⁺ oRG cluster included *FEZF2*, *NFIA*, *SYT1*, *STMN1*, *JGA1*, *BCL2*, and *HOPX* (Figure 5A; Table S5). In contrast to this, most significantly upregulated genes in HOPX⁻ oRG included *PAX6*, *FOXG1*, *FABP5*, *QKI*, and *MOXD1* (Figure 5A; Table S5). DEGs in HOPX⁻ oRG were enriched for biological processes related to cerebral cortex development, neuronal differentiation, axogenesis, microtubule cytoskeleton
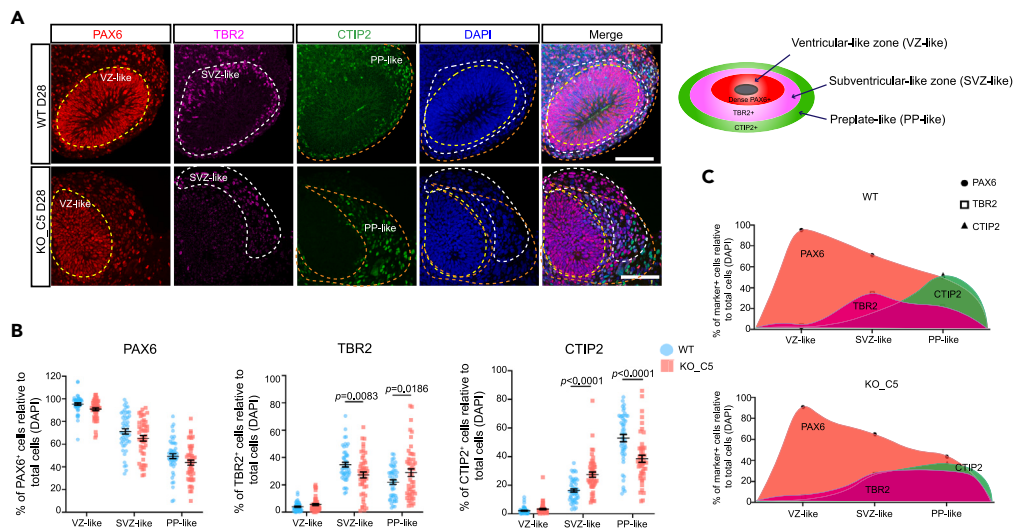
Figure 4. Cortical lamination defects were present in D28 FEZ1-null hCOs

(A) IF staining of PAX6, TBR2, and CTIP2 showed abnormal lamination in D28 FEZ1-null hCOs. Layering in WT hCOs was unaffected. Scale bar: 100 μm.

(B) Quantification of PAX6$^+$, TBR2$^+$, and CTIP2$^+$ cells in the VZ-like, SVZ-like, and PP-like in D28 WT and FEZ1-null hCOs. Values represent mean ± SEM (n = 4 independent organoid differentiations with 9 organoids for WT and FEZ1-null, respectively. Each data points represent one analyzed organoid region. At least 5 regions were analyzed within each organoid. two-way ANOVA with Šidák's multiple comparison was performed with the p values indicated).

(C) Charts showing distribution of PAX6$^+$, TBR2$^+$, and CTIP2$^+$ cells in WT versus FEZ1-null D28 hCOs based on quantification of IF images as shown in (A). In WT hCOs, TBR2$^+$, and CTIP2$^+$ regions sequentially expand from SVZ-like to PP-like. However, delineation of the 2 layers was perturbed in FEZ1-null hCOs and both cell types appeared to intermingle with each other. VZ-like: ventricular-like zone; SVZ-like: subventricular-like zone; PP-like: preplate-like.

organization, supporting the notion that the increased population of HOPX$^-$ oRG accompanying FEZ1 loss can affect early brain development (Figure 5B; Table S6). Analyses of DEGs against KEGG curated pathways further highlighted changes in expression of genes involved in MAPK signaling, regulation of actin cytoskeleton, cell adhesion molecules, tight junction, and focal adhesion (Figure S6A; Table S7). Of note, significant alterations in expression of genes involved in cell adhesion and actin cytoskeleton regulation (Figure S6B; Table S7), such as ACTB (log$_2$FC = −0.61, FDR = 9.25e-77), CDH2 (log$_2$FC = 0.393; FDR = 5.20e-24), NCAM1 (log$_2$FC = 0.22; FDR = 6.9e-12), CNTNAP2 (log$_2$FC = −2.37; FDR<1.89E-294), CNTNAP3B (log$_2$FC = −0.25; FDR = 4.17E-22), PTK2 (log$_2$FC = −0.147; FDR = 4.76E-8), MAPK10 (log$_2$FC = −0.5; FDR = 3.71E-50), MAPK3 (log$_2$FC = −0.2; FDR = 2.17E-19) were detected in HOPX$^-$ oRG (Table S5). Both signaling pathways are crucial for neuronal morphogenesis and cell migration during corticogenesis.[63–65] Additionally, significant downregulation of TMSB4X (log$_2$FC = −0.398; FDR = 1.85E-15), PFN1 (log$_2$FC = −0.212; FDR = 7.35E-09), PFN2 (log$_2$FC = −0.341; FDR = 4.31E-20), and ARPC2 (log$_2$FC = −0.162; FDR = 4.45E-6) were also observed in HOPX$^-$ oRG (Figure 5C; Table S5). These molecules are known to regulate F-actin polymerization, which is vital in modulating cell migration and neurite outgrowth of neural progenitors (Figure 5D).[65–67] Therefore, we examined whether alterations in actin dynamics were present in neuronal progenitor cells following loss of FEZ1.

Changes in actin polymerization can be assessed by measuring the ratio of depolymerized (globular [G]-actin) to polymerized (filamentous [F]-actin) actin.[65] We dissociated cells from D28 hCOs, plated them on coverslips and immunostained for G- and F-actin together with PAX6, a neuroprogenitor cell marker that has been reported to localize to RG cells (Figure 5E).[44,68,69] The G- to F-actin ratio in PAX6$^+$ RG cells was calculated by measuring total fluorescent intensities on each channel, respectively (Figure 5E). We postulated that any changes in G- to F-actin ratio in PAX6$^+$ cells between FEZ1-null and WT hCOs is likely attributed to differences in the relative proportion of HOPX$^+$ and HOPX$^-$ oRG populations. PAX6$^+$ RG cells from FEZ1-null hCOs indeed exhibited 33.6% ± 5.4% higher G- to F-actin ratio as compared to those from WT hCOs (Figure 5F). G-actin also appeared to be more enriched at the tips of processes in cells from FEZ1-null hCOs (Figure 5E). Thus, the larger proportion of HOPX$^-$ oRGs exhibiting higher levels of actin dynamics can account for layering abnormalities in FEZ1 null hCOs.

Ectopic localization and atypical cell migration of HOPX$^-$ oRG in FEZ1-null hCOs during corticogenesis

Migration of oRGs to oSVZ and PP regions during early cortical brain development is crucial for proper localization and expansion of the cortical layers.[70,71] Migration abnormalities give rise to cortical developmental disorders.[55,72] We next proceeded to investigate how the disproportionate amount of oRG with higher actin dynamics contributes to cortical layer formation abnormalities in FEZ1-null hCOs.

There is currently no reliable marker to distinguish between HOPX$^+$ versus HOPX$^-$ oRG. Since QKI was highly expressed in HOPX$^-$ but not in HOPX$^+$ oRG (Figure S4A), we employed it as a putative marker to examine the distribution of the former population of cells in D28 hCOs.[73]
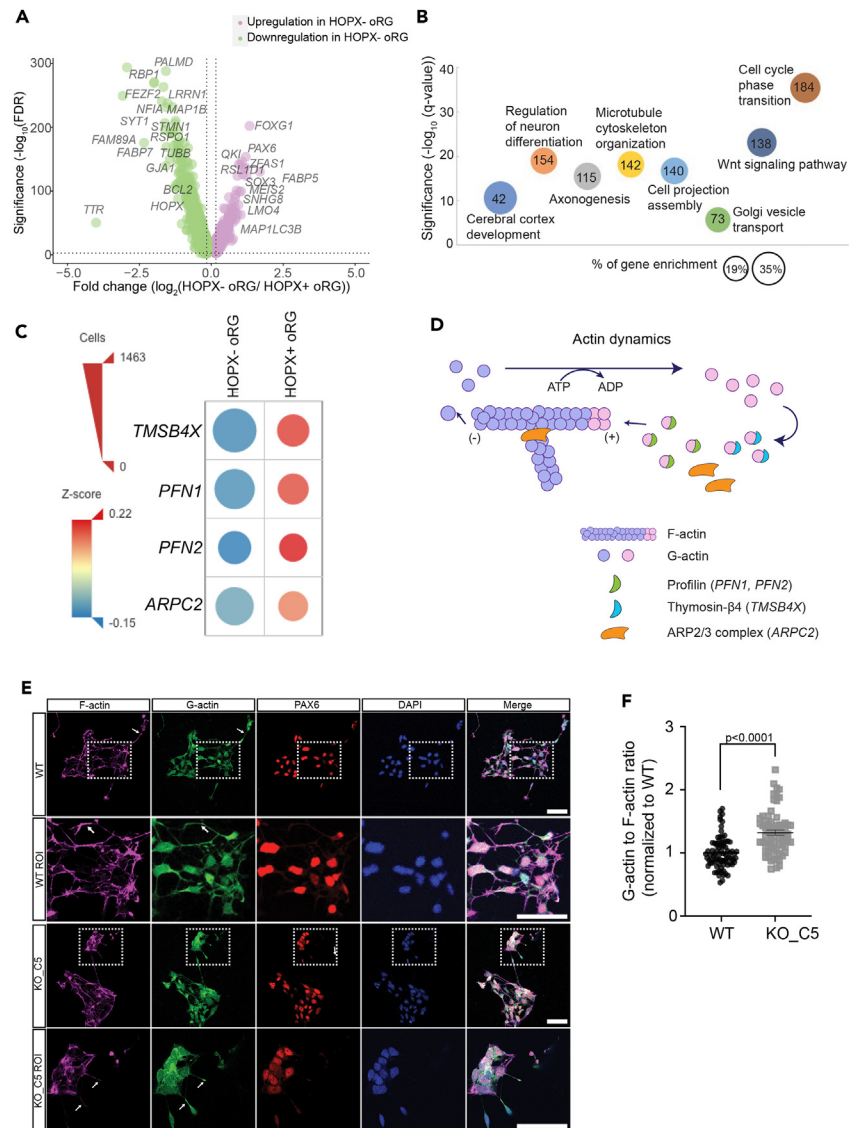
Figure 5. HOPX⁻ oRG population exhibited higher levels of actin dynamics

(A) Volcano plot of DEGs in HOPX⁻ oRGs compared with HOPX⁺ oRGs. DEGs of interest are indicated in the plot.

(B) GO enrichment analyses (by Metascape) of DEGs in HOPX⁻ oRGs as compared to HOPX⁺ oRGs. Size and number of the circles represent the percentage and number of DEGs involved in each term, respectively.

(C) Dot plot showing expression levels of DEGs involved in actin polymerization in HOPX⁻ oRGs and HOPX⁺ oRGs. Affected genes were downregulated in HOPX⁻ oRGs. Expression levels are color-coded according to their Z-scores. The diameter of each dot correlates with the number of cells (as scaled by triangular red legend) for the corresponding gene. Analysis was done using Bioturing.

(D) Diagram showing the regulation of actin dynamics. Polymerized F-actin is dissembled into monomer G-actin at the minus (−) end while G-actin is incorporated at the plus (+) end of F-actin. Profilin 1 and 2 (PFN1, PFN2), Thymosin-β4 (TMSB4X), ARP2/3 complex (ARPC2) participate in assembling monomer G-actin to polymerized F-actin.

(E) IF staining of F- and G-actin in WT and FEZ1-null PAX6⁺ neural progenitors dissociated from D28 hCOs. Arrows shows enrichment of G-actin at neurite tips in FEZ1-null neural progenitors as compared with WT. Scale bar: 100 μm.

(F) Quantification of G- to F-actin ratio in neural progenitors dissociated from D28 hCOs from WT and FEZ1-null hCOs. Values represent mean ± SEM. (n = 3 independent organoid differentiations for WT and FEZ1-null, respectively. Each data points represent measurements from one image, at least 10 images were analyzed within each replicate. Unpaired t test were performed to determine the two-tailed p value as indicated).

In WT D28 hCOs, QKI⁺ oRG were predominantly found in the VZ-like and rarely at the SVZ-like region (including the PP-like region, henceforth collectively indicated as SVZ-PP-like) (Figure 6A). This supports its expression in vRG and oRG at this stage of development.[33,47] Remarkably, the SVZ-PP-like region in D28 FEZ1-null hCOs contained significantly more of QKI⁺ oRG as compared to WT hCOs (Figure 6A). Similar results
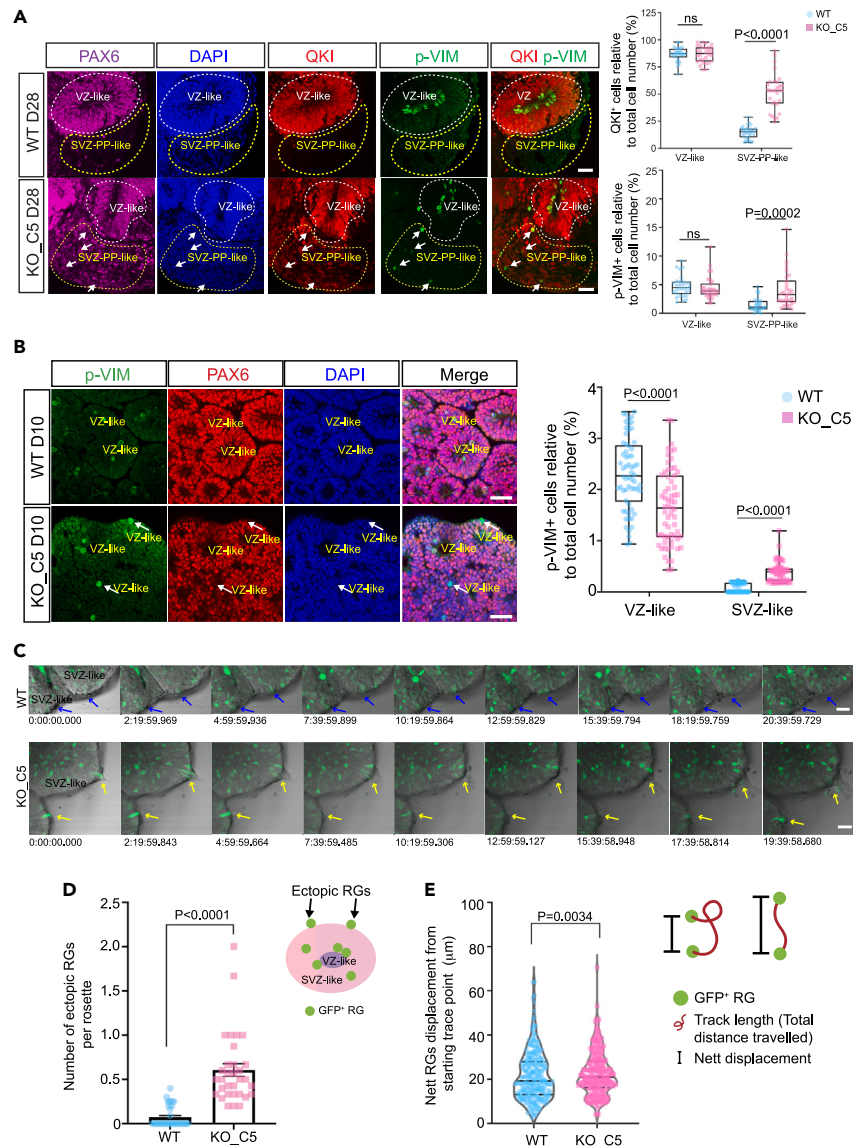
Figure 6. Ectopic localization of HOPX⁻ oRG in FEZ1-null hCOs

(A) D28 WT and FEZ1-null hCOs were stained for PAX6 (RG marker), QKI (vRG and HOPX⁻ oRG marker), and p-VIM (mitotic RG marker). In WT hCOs, QKI⁺ RGs, and mitotic RGs were largely confined within the VZ-like region. In FEZ1-null hCOs, the populations of both cell types increased dramatically in the SVZ-PP-like region. White arrows indicate pVIM⁺ mitotic RGs. Quantification of QKI⁺ and p-VIM⁺ cells are shown on the right. Scale bar: 50 μm.

(B) Ectopic mitotic RG (p-VIM⁺) could be observed at the outer surface of rosettes in D10 FEZ1-null hCOs (arrows). Quantification of p-VIM⁺ cells are shown on the right. Scale bar: 100 μm. For (A) and (B), values represent mean ± SEM (n = 3 independent organoid differentiations with 8 organoids analyzed for WT and FEZ1-null, respectively. Each data points represent one analyzed region of an organoid; at least 5 different regions were analyzed from one organoid. Unpaired t test with Welch's correction was performed, with two-tailed p values as indicated).

(C) Time lapse imaging in D10 hCOs infected with GFP-expressing AAVs showed abnormal migration of GFP⁺ RG in FEZ1-null hCOs as compared to WT hCOs. Arrows indicate labeled cells at the edge of SVZ-like region. Cells in WT hCO were confined within each rosette while undergoing proliferation or relocation (blue arrows). In contrast, some RG cells in FEZ1-null hCOs appear atypical migration behavior by migrating out of the rosettes (yellow arrow). Corresponding videos can be found in Videos S1 (D10 WT hCO migration) and S2 (D10 FEZ1-null hCO migration). Scale bar: 50 μm.

(D) Illustration and quantification of atypical cells with abnormal migration observed during time lapse recording. Values represent mean ± SEM (n = 3 independent organoid differentiations for WT and FEZ1-null, respectively. Each data points represent one analyzed region in an organoid. At least 10 different regions were analyzed within one replicate. Unpaired t test with Welch's correction was performed with two-tailed p values as indicated).

(E) Quantification of nett cell displacement. Nett displacement of GFP⁺ RGs in FEZ1-null hCOs was higher as compared to WT hCOs. Values represent mean ± SEM (n = 3 independent organoid differentiations, each data points represent one traced cell that could be consecutively traced for more than 7 h. Unpaired t test with Welch's correction was performed with two-tailed p values as indicated). VZ-like: ventricular-like zone; SVZ-PP-like: subventricular-like zone and preplate-like; SVZ-like: subventricular-like zone.
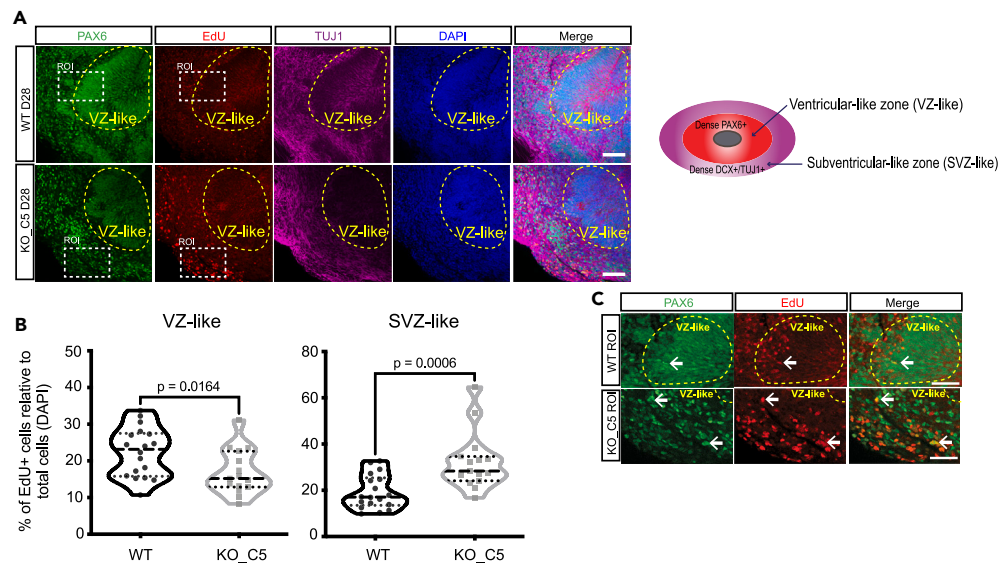
Figure 7. Ectopic localization and proliferation of RG in FEZ1-null hCOs

(A) Lineage tracing of postmitotic daughter cells on D28 hCO by EdU pulse labeling assay for both WT and FEZ1-null group with co-staining with PAX6 and TUJ1. More daughter cells were located at the SVZ-like region in FEZ1-null hCOs. Scale bar: 100 μm.

(B) Quantification of EdU$^+$ post-mitotic cells in different regions. Values are represented as violin plots with median and quartiles indicated as dashed and dotted lines, respectively. Values represent mean ± SEM (n = 3 independent organoid differentiations with 6 individual organoids for WT and FEZ1-null, respectively. Each data points represent value from one analyzed organoid region. At least 4 regions were analyzed for each organoid. Unpaired t test with Mann-Whitney test was applied to determine the indicated two-tailed p values).

(C) ROI in (A) showing that a proportion of EdU$^+$ cells are PAX6$^+$ RGs (white arrow). Scale bar: 50 μm. VZ, ventricular-like zone; SVZ, subventricular-like zone.

were observed in organoids stained with MOXD1, which is also highly expressed in HOPX$^-$ oRG. More MOXD1$^+$ cells were found in the SVZ-PP of FEZ1-null hCOs as compared to WT hCOs (Figure S7A).

We noticed that ectopic localization of QKI$^+$ oRG could already be seen in D10 FEZ1-null hCOs (Figure S7B). In WT hCOs, pVIM$^+$ mitotic RG were typically found close to the inner core of VZ-like and rarely at the edge of each rosette at both D10 and D28 WT hCOs (Figures 6A and 6B). However, the ectopic pVIM$^+$ mitotic RG were often detected at the outer edge of rosettes in D10 FEZ1-null hCOs, with a concomitant reduction in the number of VZ-associated mitotic RGs (Figure 6B). This population of ectopic pVIM$^+$ RGs in the SVZ-PP-like region persisted as the FEZ1-null hCOs developed (Figure 6A, D28), therefore indicating loss of FEZ1 not only resulted in an increase and persistence of HOPX$^-$ oRGs, but also in their ectopic localization to the SVZ-PP-like regions of the hCOs.

As our previous scRNA-seq data highlighted differences in actin dynamics between HOPX$^-$ and HOPX$^+$ oRG, we further examined whether the ectopically localized oRG population exhibited abnormal cell migratory behavior by infecting D10 FEZ1-null and WT hCOs with a low titer of GFP-expressing AAVs to sparsely label cells. We tracked the migration of GFP$^+$ cells over a 20-h period by time-lapsed imaging. In day 10 hCOs, most of the cells were PAX6$^+$ and QKI$^+$ (Figure S7B), most cells present at this stage are presumed to be dominantly of RG cell identity.[44,68,69] In agreement with the presence of an expanded population of HOPX$^-$ oRG cells with higher actin dynamics with FEZ1 loss, a higher proportion of migrating GFP-labeled cells could be observed to move to the outer edge of rosettes in FEZ1-null hCOs (yellow arrow) versus WT hCOs (Figures 6C, 6D, and S8). Interestingly, more GFP$^+$ cells in mutant hCOs could be consecutively tracked for more than 7 h, which suggested that they exhibited more persistent migratory behavior than those in WT hCOs (Figures S7C and S8; Videos S1 (WT) and S2 [FEZ1-null]). Additionally, these cells in FEZ1-null hCOs showed greater displacement (Figure 6E) and appear to remain at the periphery, even though track length (total distance traveled) and migration speed did not show significant difference as compared to WT cells (Figures S7D and S7E).

Previous studies indicated HOPX$^-$ oRG possessed both self-renewal capability and were able to further differentiate into IP and other neuronal cell types.[44] To further investigate how ectopic HOPX$^-$ oRG could affect cortical layering, we tested the self-renewal capability of these cells by pulse labeling the organoids with 5-ethynyl-2'-deoxyuridine (EdU) on D23 and harvesting them on D28, when HOPX$^-$ oRG population can be detected in SVZ-like region (Figure 7A). We defined the dense PAX6$^+$ region as VZ-like and the region that was strongly labeled for TUJ1 or DCX surrounding the VZ-like as SVZ-like[31,34,74] (Figures 7A and S9A). We quantified number of EdU$^+$ cells in VZ-like and SVZ-like regions and found that there were more EdU$^+$ post-mitotic cells observed in the SVZ-like region of FEZ1-null hCOs compared to WT hCOs (Figure 7B). The number of cells counted per area was consistent across different regions of hCOs (Figure S9B). A portion of these cells also stained positive for PAX6 (Figure 7C, arrows). We next determined where cell proliferation occurs by staining for Ki67. Increased amount of mislocalized mitotic (Ki67$^+$) cells in SVZ-like of FEZ1-null hCOs was observed (Figures S9C and S9D). A proportion of Ki67$^+$ cells were also PAX6$^+$ (Figure S9C, arrow). Together with the earlier results showing localization of ectopic HOPX$^-$ oRG, these

data indicated that abnormal migration and subsequent division of mislocalized oRG eventually resulted in abnormalities in cortical layer formation in FEZ1-null hCOs.

DISCUSSION

Using hCOs as a model of human brain development, we demonstrated that *FEZ1* expression was switched on early during cortical development as hESCs differentiated into neuroprogenitor cell types. FEZ1 levels continued to increase in major subsets of neuroprogenitors and were almost universally expressed in immature neurons. Deleting *FEZ1* significantly altered the expression of other genes involved in neuronal development and synaptic function. Remarkably, FEZ1 deficiency disrupted the ratio of HOPX$^+$ and HOPX$^-$ oRG, with HOPX$^-$ oRG being substantially increased and HOPX$^+$ oRG being decreased in FEZ1-null hCOs. FEZ1-null HOPX$^-$ oRG displayed differential expression of genes that regulate actin dynamics. Supporting the expansion of this oRG subtype, neuroprogenitor cells in FEZ1-null organoids exhibited increased levels of actin dynamics and had a higher tendency to migrate to the peripheral edge of the organoids. This observation was suggestive of altered cell migration patterns in FEZ1-null hCOs, which were supported by greater inter-mixing of TBR2$^+$ intermediate progenitor cells with CTIP2$^+$ deep layer neurons in FEZ1-null hCOs, indicative of abnormalities of early cortical layer formation. Collectively, these results highlight a hitherto unknown role of FEZ1 during the early stages of brain development.

Although previous reports highlighted the involvement of FEZ1 in neuronal and synaptic development, its involvement in the earlier stages of brain development has never been fully explored.[8,9,14,75] Detection of *FEZ1* transcripts early in rodent brain development and the association of *FEZ1* mutations in human neurodevelopmental disorders indicate the possibility of its involvement at even earlier stages of brain development.[76] Indeed, *FEZ1* mRNA and protein were already present as early as D10 in hCOs, which is equivalent to a 4-5 weeks-old human embryo and an E11 mouse embryo.[29,41,77] Moreover, scRNA-seq and confocal microscopy analyses further localized *FEZ1* expression to distinct subsets of neuroprogenitor cells, including NE, vRG, oRG, and, later, in newborn as well as immature neurons.

Early in the course of neurogenesis, progressive expansion and differentiation of NE to vRG, oRG, and IP are responsible for producing the vast diversity of cortical neurons and subsequent organized expansion of cortical layers.[33,42,78,79] oRGs play a pivotal role during the development of the human cortex by producing intermediate progenitor cells (IP), which in turn give rise to neurons and various types of glial cells, contributing to cortical expansion and lamination, and the eventual formation of different cerebral regions.[54] oRGs in the OSVZ can be further distinguished into 2 subtypes by the selective expression of *HOPX*. HOPX$^+$ oRG form the larger proportion that is present in human OSVZ.[33,44] Loss of *FEZ1* appears to mainly affect oRG. A substantial increase in the proportion of HOPX$^-$ oRG, accompanied by a corresponding decrease in HOPX$^+$ oRG was detected in FEZ1-null hCOs as compared to WT hCOs. HOPX$^+$ oRG and HOPX$^-$ oRG show differences in their ability to generate TBR2$^+$ IP.[44] The shift in both quantity and proportion of both oRG types was accompanied by a disproportionate increase in TBR2$^+$ IP and reduction in CTIP2$^+$ deep layer neurons and encroachment of IP into the deep layer neuron layer. In agreement with this, our scRNA-seq data uncovered an increase in the TBR2$^+$ IP population in FEZ1-null hCOs (Figure 3). Moreover, upregulation of EOMES/TBR2 and INSM1 (upstream of TBR2 signaling), and downregulation of ZNFPM2/FOG2 (the layer 6 marker and downstream of TBR2 signaling) were observed in FEZ1-null hCOs compared with WT (Table S5), indicating aberrant IP production and transition to deep layer neurons in FEZ1-null hCOs.[80–83] These results are reminiscent of abnormalities observed in *Bcl11a/CTIP1*-deficient mice, where a significant bias in specification and generation of subcerebral projection neurons and impaired neuronal radial migration was observed.[82,83] Nevertheless, the significance of this relationship is at the moment unclear and is an important question for further investigation.

Apart from abnormalities in generation of neuroprogenitor subtypes, alterations in RG migration can also affect cortical formation.[84,85] Mispositioning of oRGs as a result of dysregulated mammalian target of rapamycin (mTOR) signaling has been identified to affect oRG migration by changing their actin cytoskeleton through Rho-GTPase and CDC42.[86] Although HOPX$^+$ and HOPX$^-$ oRG are both implicated in cortical expansion; differences between both cell types remain unclear.[42,44,57,58] Nevertheless, differences in actin cytoskeleton regulation has been suggested to contribute to differences in migration behavior between the HOPX$^+$ and HOPX$^-$ oRG.[86,87] Our examination of DEGs in HOPX$^-$ oRG versus HOPX$^+$ oRG also found changes in the expression of genes regulating actin dynamics, which generate protrusive and contractile motion involved in cell migration, especially during soma translocation.[67,88] The dynamics of stabilized and destabilized F-actin at the leading process tip of the cell provided pulling forces to drive nucleus moving, therefore to control cell migration and position.[88]

While FEZ1's function has been closely linked to microtubule-base intracellular transport, its association with the actin cytoskeleton has also been previously reported. FEZ1 was copurified with F-actin, through which it recruits DISC1.[75] DISC1 has been shown to modulate neuronal migration through its interaction with actin cytoskeleton related proteins that either facilitate or inhibit neural migration, such as NDEL1, ACTB, AKT1, and GIRDIN.[88–90] Hence, FEZ1 could exert its effect on the actin cytoskeleton and cell migration via its interaction with DISC1.[75,88] Additionally, FEZ1 colocalized with actin in the tips of growing processes in oligodendroglia progenitor cells.[91] Knocking down *FEZ1* expression in these cells significantly reduced the growth of these processes, suggesting that FEZ1 could be involved in regulating cell migration behavior. Thus, together with the expanded population, higher levels of actin dynamics in HOPX$^-$ oRG neuroprogenitors can account for the greater anomalous migration of neuroprogenitors toward the outer periphery of organoids observed in FEZ1-null hCOs.

In conclusion, our study uncovered the importance of FEZ1 during early forebrain development in terms of neurogenesis, neural specification, and cortical brain deep layer stratification. These findings potentially contribute toward the understanding of neural developmental pathologies underlying neuropsychiatric disorders, therefore paving the way for potential treatment approaches.

Limitations of the study

A limitation of this study is that we have not been able to directly stain for oRGs in hCOs. It would be important to investigate this further in future studies. Another important area for additional studies would be to assess the effect of FEZ1 in the morphology of developing human neurons since its deletion has been linked to abnormalities in axodendritic development in other model organisms.

STAR★METHODS

Detailed methods are provided in the online version of this paper and include the following:

- KEY RESOURCES TABLE
- RESOURCE AVAILABILITY
  - ○ Lead contact
  - ○ Materials availability
  - ○ Data and code availability
- EXPERIMENTAL MODEL AND STUDY PARTICIPANT DETAILS
  - ○ Human ESC line and iPSC line (hPSC lines)
- METHOD DETAILS
  - ○ Generation of FEZ1 knockout (KO) hPSC lines by CRISPR/CAS9
  - ○ Genomic sequencing of FEZ1 knockout (KO) hPSC lines
  - ○ 2D neural epithelium (NE) induction
  - ○ Generation of human cerebral organoids (hCOs)
  - ○ Immunofluorescence (IF) microscopy
  - ○ EdU labeling
  - ○ Protein sample preparation and immunoblot assays
  - ○ Cell migration studies in hCOs
  - ○ Bulk RNA sequence (RNA-seq) sample preparation and RT-PCR
  - ○ Single-cell RNA sequencing (scRNA-seq)
  - ○ Bulk RNA-seq analysis
  - ○ scRNA-seq analysis
  - ○ F-actin and G-actin assays
  - ○ Quantification of IF images
  - ○ Quantification of cell migration
- QUANTIFICATION AND STATISTICAL ANALYSIS

SUPPLEMENTAL INFORMATION

Supplemental information can be found online at https://doi.org/10.1016/j.isci.2023.108497.

AUTHOR CONTRIBUTIONS

Conceptualization, Y.C.T. and J.J.E.C.; investigation: Y.H.Q, J.J.Y.L., and O.A.; resources and data curation, O.A. and H.Y.; writing – original draft, Y.H.Q., Y.C.T., and J.J.E.C.; writing – review & editing, Y.H.Q., J.J.Y.L., O.A., H.Y., Y.C.T., and J.J.E.C.; supervision, Y.C.T. and J.J.E.C.; funding acquisition, J.J.E.C.

DECLARATION OF INTERESTS

The authors declare no competing interests.

INCLUSION AND DIVERSITY

We support inclusive, diverse, and equitable conduct of research.

REFERENCES

1. Paridaen, J.T.M.L., and Huttner, W.B. (2014). Neurogenesis during development of the vertebrate central nervous system. EMBO Rep. 15, 351–364.

2. Silbereis, J.C., Pochareddy, S., Zhu, Y., Li, M., and Sestan, N. (2016). The Cellular and Molecular Landscapes of the Developing Human Central Nervous System. Neuron 89, 248–268.

3. Lui, J.H., Hansen, D.V., and Kriegstein, A.R. (2011). Development and Evolution of the Human Neocortex (Elsevier).

4. Klingler, E., Francis, F., Jabaudon, D., and Cappello, S. (2021). Mapping the molecular and cellular complexity of cortical malformations. Science 371, eaba4517.

5. Gandal, M.J., Haney, J.R., Parikshak, N.N., Leppa, V., Ramaswami, G., Hartl, C., Schork, A.J., Appadurai, V., Buil, A., Werge, T.M., et al. (2018). Shared molecular neuropathology across major psychiatric disorders parallels polygenic overlap. Science 359, 693–697.

6. Walker, R.L., Ramaswami, G., Hartl, C., Mancuso, N., Gandal, M.J., de la Torre-Ubieta, L., Pasaniuc, B., Stein, J.L., and Geschwind, D.H. (2019). Genetic Control of Expression and Splicing in Developing Human Brain Informs Disease Mechanisms. Cell 179, 750–771.e22.

7. Rosato, M., Stringer, S., Gebuis, T., Paliukhovich, I., Li, K.W., Posthuma, D., Sullivan, P.F., Smit, A.B., and van Kesteren, R.E. (2021). Combined cellomics and proteomics analysis reveals shared neuronal morphology and molecular pathway phenotypes for multiple schizophrenia risk genes. Mol. Psychiatry 26, 784–799.

8. Bloom, L., and Horvitz, H.R. (1997). The Caenorhabditis elegans gene unc-76 and its human homologs define a new gene family involved in axonal outgrowth and fasciculation. Proc. Natl. Acad. Sci. USA 94, 3414–3419.

9. Butkevich, E., Härtig, W., Nikolov, M., Erck, C., Grosche, J., Urlaub, H., Schmidt, C.F., Klopfenstein, D.R., and Chua, J.J.E. (2016). Phosphorylation of FEZ1 by Microtubule Affinity Regulating Kinases regulates its function in presynaptic protein trafficking. Sci. Rep. 6, 1–15.

10. Desai, C., Garriga, G., McIntire, S.L., and Horvitz, H.R. (1988). A genetic pathway for the development of the Caenorhabditis elegans HSN motor neurons. Nature 336, 638–646.

11. Su, C.W., Tharin, S., Jin, Y., Wightman, B., Spector, M., Meili, D., Tsung, N., Rhiner, C., Bourikas, D., Stoeckli, E., et al. (2006). The short coiled-coil domain-containing protein UNC-69 cooperates with UNC-76 to regulate axonal outgrowth and normal presynaptic organization in Caenorhabditis elegans. J. Biol. 5, 9.

12. Gindhart, J.G., Chen, J., Faulkner, M., Gandhi, R., Doerner, K., Wisniewski, T., and Nandlestadt, A. (2003). The kinesin-associated protein UNC-76 is required for axonal transport in the Drosophila nervous system. Mol. Biol. Cell 14, 3356–3365.

13. Toda, H., Mochizuki, H., Flores, R., 3rd, Josowitz, R., Krasieva, T.B., Lamorte, V.J., Suzuki, E., Gindhart, J.G., Furukubo-Tokunaga, K., and Tomoda, T. (2008). UNC-51/ATG1 kinase regulates axonal transport by mediating motor-cargo assembly. Genes Dev. 22, 3292–3307.

14. Chua, J.Y., Ng, S.J., Yagensky, O., Wanker, E.E., and Chua, J.J.E. (2021). FEZ1 forms complexes with CRMP1 and DCC to regulate axon and dendrite development. eNeuro 8, ENEURO.0193-20.2021.

15. Kang, E., Burdick, K.E., Kim, J.Y., Duan, X., Guo, J.U., Sailor, K.A., Jung, D.E., Ganesan, S., Choi, S., Pradhan, D., et al. (2011). Interaction between FEZ1 and DISC1 in regulation of neuronal development and risk for schizophrenia. Neuron 72, 559–571.

16. Gunaseelan, S., Wang, Z., Tong, V.K.J., Ming, S.W.S., Razar, R.B.B.A., Srimasorn, S., Ong, W.-Y., Lim, K.-L., and Chua, J.J.E. (2021). Loss of FEZ1, a gene deleted in Jacobsen syndrome, causes locomotion defects and early mortality by impairing motor neuron development. Hum. Mol. Genet. 30, 5–20.

17. Sakae, N., Yamasaki, N., Kitaichi, K., Fukuda, T., Yamada, M., Yoshikawa, H., Hiranita, T., Tatsumi, Y., Kira, J.I., Yamamoto, T., et al. (2008). Mice lacking the schizophrenia-associated protein FEZ1 manifest hyperactivity and enhanced responsiveness to psychostimulants. Hum. Mol. Genet. 17, 3191–3203.

18. Sumitomo, A., Saka, A., Ueta, K., Horike, K., Hirai, K., Gamo, N.J., Hikida, T., Nakayama, K.I., Sawa, A., Sakurai, T., and Tomoda, T. (2018). Methylphenidate and Guanfacine Ameliorate ADHD-Like Phenotypes in Fez1-Deficient Mice. Mol. Neuropsychiatry 3, 223–233.

19. Favier, R., Akshoomoff, N., Mattson, S., and Grossfeld, P. (2015). Jacobsen syndrome: Advances in our knowledge of phenotype and genotype. Am. J. Med. Genet. C Semin. Med. Genet. 169, 239–250.

20. Grossfeld, P.D., Mattina, T., Lai, Z., Favier, R., Jones, K.L., Cotter, F., and Jones, C. (2004). The 11q terminal deletion disorder: a prospective study of 110 cases. Am. J. Med. Genet. 129A, 51–61.

21. Mattina, T., Perrotta, C.S., and Grossfeld, P. (2009). Jacobsen syndrome. Orphanet J. Rare Dis. 4, 9.

22. Colantuoni, C., Hyde, T.M., Mitkus, S., Joseph, A., Sartorius, L., Aguirre, C., Creswell, J., Johnson, E., Deep-Soboslay, A., Herman, M.M., et al. (2008). Age-related changes in the expression of schizophrenia susceptibility genes in the human prefrontal cortex. Brain Struct. Funct. 213, 255–271.

23. Lipska, B.K., Peters, T., Hyde, T.M., Halim, N., Horowitz, C., Mitkus, S., Weickert, C.S., Matsumoto, M., Sawa, A., Straub, R.E., et al. (2006). Expression of DISC1 binding partners is reduced in schizophrenia and associated with DISC1 SNPs. Hum. Mol. Genet. 15, 1245–1258.

24. Tang, J., Fan, Y., Li, H., Xiang, Q., Zhang, D.F., Li, Z., He, Y., Liao, Y., Wang, Y., He, F., et al. (2017). Whole-genome sequencing of monozygotic twins discordant for schizophrenia indicates multiple genetic risk factors for schizophrenia. J. Genet. Genom. 44, 295–306.

25. Vachev, T.I., Stoyanova, V.K., Ivanov, H.Y., Minkov, I.N., and Popov, N.T. (2015). Investigation of fasciculation and elongation protein zeta-1 (FEZ1) in peripheral blood reveals differences in gene expression in patients with schizophrenia. Balkan J. Med. Genet. 18, 31–38.

26. Yamada, K., Nakamura, K., Minabe, Y., Iwayama-Shigeno, Y., Takao, H., Toyota, T., Hattori, E., Takei, N., Sekine, Y., Suzuki, K., et al. (2004). Association analysis of FEZ1 variants with schizophrenia in Japanese cohorts. Biol. Psychiatry 56, 683–690.

27. Jurcă, A.D., Kozma, K., Ioana, M., Streață, I., Petcheși, C.D., Bembea, M., Jurcă, M.C., Cuc, E.A., Vesa, C.M., and Buhaş, C.L. (2017). Morphological and genetic abnormalities in a Jacobsen syndrome. Rom. J. Morphol. Embryol. 58, 1531–1534.

28. Tyson, C., Qiao, Y., Harvard, C., Liu, X., Bernier, F.P., McGillivray, B., Farrell, S.A., Arbour, L., Chudley, A.E., Clarke, L., et al. (2008). Submicroscopic deletions of 11q24-25 in individuals without Jacobsen syndrome: re-examination of the critical region by high-resolution array-CGH. Mol. Cytogenet. 1, 23.

29. Fujita, T., Ikuta, J., Hamada, J., Okajima, T., Tatematsu, K., Tanizawa, K., and Kuroda, S. (2004). Identification of a tissue-non-specific homologue of axonal fasciculation and elongation protein zeta-1. Biochem. Biophys. Res. Commun. 313, 738–744.

30. Lancaster, M.A., and Knoblich, J.A. (2014). Generation of cerebral organoids from human pluripotent stem cells. Nat. Protoc. 9, 2329–2340.

31. Qian, X., Nguyen, H.N., Song, M.M., Hadiono, C., Ogden, S.C., Hammack, C., Yao, B., Hamersky, G.R., Jacob, F., Zhong, C., et al. (2016). Brain-Region-Specific Organoids Using Mini-bioreactors for Modeling ZIKV Exposure. Cell 165, 1238–1254.

32. Lancaster, M.A., Renner, M., Martin, C.-A., Wenzel, D., Bicknell, L.S., Hurles, M.E., Homfray, T., Penninger, J.M., Jackson, A.P., and Knoblich, J.A. (2013). Cerebral organoids model human brain development and microcephaly. Nature 501, 373–379.

33. Pollen, A.A., Nowakowski, T.J., Chen, J., Retallack, H., Sandoval-Espinosa, C., Nicholas, C.R., Shuga, J., Liu, S.J., Oldham, M.C., Diaz, A., et al. (2015). Molecular Identity of Human Outer Radial Glia during Cortical Development. Cell 163, 55–67.

34. Renner, M., Lancaster, M.A., Bian, S., Choi, H., Ku, T., Peer, A., Chung, K., and Knoblich, J.A. (2017). Self-organized developmental

patterning and differentiation in cerebral organoids. EMBO J. *36*, 1316–1329.

35. Mora-Bermúdez, F., Badsha, F., Kanton, S., Camp, J.G., Vernot, B., Köhler, K., Voigt, B., Okita, K., Maricic, T., He, Z., et al. (2016). Differences and similarities between human and chimpanzee neural progenitors during cerebral cortex development. Elife *5*, e18683.

36. Ying, Q.L., Stavridis, M., Griffiths, D., Li, M., and Smith, A. (2003). Conversion of embryonic stem cells into neuroectodermal precursors in adherent monoculture. Nat. Biotechnol. *21*, 183–186.

37. Dong, F., Mao, J., Chen, M., Yoon, J., and Mao, Y. (2021). Schizophrenia risk ZNF804A interacts with its associated proteins to modulate dendritic morphology and synaptic development. Mol. Brain *14*, 12.

38. Grigoryan, T., Stein, S., Qi, J., Wende, H., Garratt, A.N., Nave, K.A., Birchmeier, C., and Birchmeier, W. (2013). Wnt/Rspondin/beta-catenin signals control axonal sorting and lineage progression in Schwann cell development. Proc. Natl. Acad. Sci. USA *110*, 18174–18179.

39. Mulligan, K.A., and Cheyette, B.N.R. (2012). Wnt signaling in vertebrate neural development and function. J. Neuroimmune Pharmacol. *7*, 774–787.

40. Sun, Y., Lu, X.j., Fu, X., Zhang, Y., Zhan, Y., Liu, J., Zhao, L., and Xia, C.l. (2021). Engrafted primary type-2 astrocytes improve the recovery of the nigrostriatal pathway in a rat model of Parkinson's disease. Mol. Cell. Biochem. *476*, 619–631.

41. Camp, J.G., Badsha, F., Florio, M., Kanton, S., Gerber, T., Wilsch-Bräuninger, M., Lewitus, E., Sykes, A., Hevers, W., Lancaster, M., et al. (2015). Human cerebral organoids recapitulate gene expression programs of fetal neocortex development. Proc. Natl. Acad. Sci. USA *112*, 15672–15677.

42. Nowakowski, T.J., Bhaduri, A., Pollen, A.A., Alvarado, B., Mostajo-Radji, M.A., Di Lullo, E., Haeussler, M., Sandoval-Espinosa, C., Liu, S.J., Velmeshev, D., et al. (2017). Spatiotemporal gene expression trajectories reveal developmental hierarchies of the human cortex. Science *358*, 1318–1323.

43. Bhaduri, A., Andrews, M.G., Mancia Leon, W., Jung, D., Shin, D., Allen, D., Jung, D., Schmunk, G., Haeussler, M., Salma, J., et al. (2020). Cell stress in cortical organoids impairs molecular subtype specification. Nature *578*, 142–148.

44. Matsumoto, N., Tanaka, S., Horiike, T., Shinmyo, Y., and Kawasaki, H. (2020). A discrete subtype of neural progenitor crucial for cortical folding in the gyrencephalic mammalian brain. Elife *9*, e54873.

45. Schulmann, A., Marenco, S., Vawter, M.P., Akula, N., Limon, A., Mandal, A., Auluck, P.K., Patel, Y., Lipska, B.K., and McMahon, F.J. (2023). Antipsychotic drug use complicates assessment of gene expression changes associated with schizophrenia. Transl. Psychiatry *13*, 93.

46. Wang, W.Z., Oeschger, F.M., Montiel, J.F., García-Moreno, F., Hoerder-Suabedissen, A., Krubitzer, L., Ek, C.J., Saunders, N.R., Reim, K., Villalón, A., and Molnár, Z. (2011). Comparative aspects of subplate zone studied with gene expression in sauropsids and mammals. Cereb. Cortex *21*, 2187–2203.

47. Hayakawa-Yano, Y., Suyama, S., Nogami, M., Yugami, M., Koya, I., Furukawa, T., Zhou, L., Abe, M., Sakimura, K., Takebayashi, H., et al. (2017). An RNA-binding protein, Qki5, regulates embryonic neural stem cells through pre-mRNA processing in cell adhesion signaling. Genes Dev. *31*, 1910–1925.

48. Ji, Z., and Ji, H. (2016). TSCAN: Pseudo-time reconstruction and evaluation in single-cell RNA-seq analysis. Nucleic Acids Res. *44*, e117.

49. Yu, X.X., Qiu, W.L., Yang, L., Zhang, Y., He, M.Y., Li, L.C., and Xu, C.R. (2019). Defining multistep cell fate decision pathways during pancreatic development at single-cell resolution. EMBO J. *38*, e100164.

50. Haskell, G.T., and LaMantia, A.S. (2005). Retinoic acid signaling identifies a distinct precursor population in the developing and adult forebrain. J. Neurosci. *25*, 7636–7647.

51. Penisson, M., Ladewig, J., Belvindrah, R., and Francis, F. (2019). Genes and Mechanisms Involved in the Generation and Amplification of Basal Radial Glial Cells. Front. Cell. Neurosci. *13*, 381.

52. Beattie, R., and Hippenmeyer, S. (2017). Mechanisms of radial glia progenitor cell lineage progression. FEBS Lett. *591*, 3993–4008.

53. Florio, M., and Huttner, W.B. (2014). Neural progenitors, neurogenesis and the evolution of the neocortex. Development *141*, 2182–2194.

54. Molnár, Z., Clowry, G.J., Šestan, N., Alzu'bi, A., Bakken, T., Hevner, R.F., Hüppi, P.S., Kostović, I., Rakic, P., Anton, E.S., et al. (2019). New insights into the development of the human cerebral cortex. J. Anat. *235*, 432–451.

55. Juric-Sekhar, G., and Hevner, R.F. (2019). Malformations of Cerebral Cortex Development: Molecules and Mechanisms. Annu. Rev. Pathol. *14*, 293–318.

56. Romero, D.M., Bahi-Buisson, N., and Francis, F. (2018). Genetics and mechanisms leading to human cortical malformations. Semin. Cell Dev. Biol. *76*, 33–75.

57. Liu, J., Liu, W., Yang, L., Wu, Q., Zhang, H., Fang, A., Li, L., Xu, X., Sun, L., Zhang, J., et al. (2017). The Primate-Specific Gene TMEM14B Marks Outer Radial Glia Cells and Promotes Cortical Expansion and Folding. Cell Stem Cell *21*, 635–649.e8.

58. Tabata, H., Hachiya, T., Nagata, K.I., Sakakibara, Y., and Nakajima, K. (2013). Screening for candidate genes involved in the production of mouse subventricular zone proliferative cells and an estimation of their changes in evolutionary pressure during primate evolution. Front. Neuroanat. *7*, 24.

59. Bershteyn, M., Nowakowski, T.J., Pollen, A.A., Di Lullo, E., Nene, A., Wynshaw-Boris, A., and Kriegstein, A.R. (2017). Human iPSC-Derived Cerebral Organoids Model Cellular Features of Lissencephaly and Reveal Prolonged Mitosis of Outer Radial Glia. Cell Stem Cell *20*, 435–449.e4.

60. Le, T., Phan, T., Pham, M., Tran, D., Lam, L., Nguyen, T., Truong, T., Vuong, H., Luu, T., Phung, N., et al. (2020). BBrowser: Making single-cell data easily accessible. Preprint at bioRxiv *2020*.

61. Korthauer, K.D., Chu, L.F., Newton, M.A., Li, Y., Thomson, J., Stewart, R., and Kendziorski, C. (2016). A statistical approach for identifying differential distributions in single-cell RNA-seq experiments. Genome Biol. *17*, 222.

62. Wang, T., Li, B., Nelson, C.E., and Nabavi, S. (2019). Comparative analysis of differential gene expression analysis tools for single-cell RNA sequencing data. BMC Bioinf. *20*, 40.

63. Solecki, D.J., Trivedi, N., Govek, E.E., Kerekes, R.A., Gleason, S.S., and Hatten, M.E. (2009). Myosin II motors and F-actin dynamics drive the coordinated movement of the centrosome and soma during CNS glial-guided neuronal migration. Neuron *63*, 63–80.

64. Vicente-Manzanares, M., Choi, C.K., and Horwitz, A.R. (2009). Integrins in cell migration–the actin connection. J. Cell Sci. *122*, 199–206.

65. Huang, R., Yuan, D.J., Li, S., Liang, X.S., Gao, Y., Lan, X.Y., Qin, H.M., Ma, Y.F., Xu, G.Y., Schachner, M., et al. (2020). NCAM regulates temporal specification of neural progenitor cells via profilin2 during corticogenesis. J. Cell Biol. *219*, e201902164.

66. Padmanabhan, K., Grobe, H., Cohen, J., Soffer, A., Mahly, A., Adir, O., Zaidel-Bar, R., and Luxenburg, C. (2020). Thymosin beta4 is essential for adherens junction stability and epidermal planar cell polarity. Development *147*, dev193425.

67. Schaks, M., Giannone, G., and Rottner, K. (2019). Actin dynamics in cell migration. Essays Biochem. *63*, 483–495.

68. Hansen, D.V., Lui, J.H., Parker, P.R.L., and Kriegstein, A.R. (2010). Neurogenic radial glia in the outer subventricular zone of human neocortex. Nature *464*, 554–561.

69. Götz, M., Stoykova, A., and Gruss, P. (1998). Pax6 controls radial glia differentiation in the cerebral cortex. Neuron *21*, 1031–1044.

70. Marín, O., Valiente, M., Ge, X., and Tsai, L.H. (2010). Guiding neuronal cell migrations. Cold Spring Harb. Perspect. Biol. *2*, a001834.

71. Taverna, E., Götz, M., and Huttner, W.B. (2014). The cell biology of neurogenesis: toward an understanding of the development and evolution of the neocortex. Annu. Rev. Cell Dev. Biol. *30*, 465–502.

72. Silva, C.G., Peyre, E., and Nguyen, L. (2019). Cell migration promotes dynamic cellular interactions to control cerebral cortex morphogenesis. Nat. Rev. Neurosci. *20*, 318–329.

73. Uzquiano, A., Kedaigle, A.J., Pigoni, M., Paulsen, B., Adiconis, X., Kim, K., Faits, T., Nagaraja, S., Antón-Bolaños, N., Gerhardinger, C., et al. (2022). Proper acquisition of cell class identity in organoids allows definition of fate specification programs of the human cerebral cortex. Cell *185*, 3770–3788.e27.

74. Li, Y., Muffat, J., Omer, A., Bosch, I., Lancaster, M.A., Sur, M., Gehrke, L., Knoblich, J.A., and Jaenisch, R. (2017). Induction of Expansion and Folding in Human Cerebral Organoids. Cell Stem Cell *20*, 385–396.e3.

75. Miyoshi, K., Honda, A., Baba, K., Taniguchi, M., Oono, K., Fujita, T., Kuroda, S., Katayama, T., and Tohyama, M. (2003). Disrupted-In-Schizophrenia 1, a candidate gene for schizophrenia, participates in neurite outgrowth. Mol. Psychiatry *8*, 685–694.

76. Razar, R.B.B.A., Qu, Y., Gunaseelan, S., and Chua, J.J.E. (2022). The importance of fasciculation and elongation protein zeta-1 in neural circuit establishment and

neurological disorders. Neural Regen. Res. *17*, 1165–1171.

77. Bystron, I., Rakic, P., Molnár, Z., and Blakemore, C. (2006). The first neurons of the human cerebral cortex. Nat. Neurosci. *9*, 880–886.

78. Greig, L.C., Woodworth, M.B., Galazo, M.J., Padmanabhan, H., and Macklis, J.D. (2013). Molecular logic of neocortical projection neuron specification, development and diversity. Nat. Rev. Neurosci. *14*, 755–769.

79. Gertz, C.C., Lui, J.H., LaMonica, B.E., Wang, X., and Kriegstein, A.R. (2014). Diverse behaviors of outer radial glia in developing ferret and human cortex. J. Neurosci. *34*, 2559–2570.

80. Mihalas, A.B., Elsen, G.E., Bedogni, F., Daza, R.A.M., Ramos-Laguna, K.A., Arnold, S.J., and Hevner, R.F. (2016). Intermediate Progenitor Cohorts Differentially Generate Cortical Layers and Require Tbr2 for Timely Acquisition of Neuronal Subtype Identity. Cell Rep. *16*, 92–105.

81. Cánovas, J., Berndt, F.A., Sepúlveda, H., Aguilar, R., Veloso, F.A., Montecino, M., Oliva, C., Maass, J.C., Sierralta, J., and Kukuljan, M. (2015). The specification of cortical subcerebral projection neurons depends on the direct repression of TBR1 by CTIP1/BCL11a. J. Neurosci. *35*, 7552–7564.

82. Wiegreffe, C., Simon, R., Peschkes, K., Kling, C., Strehle, M., Cheng, J., Srivatsa, S., Liu, P., Jenkins, N.A., Copeland, N.G., et al. (2015). Bcl11a (Ctip1) Controls Migration of Cortical Projection Neurons through Regulation of Sema3c. Neuron *87*, 311–325.

83. Woodworth, M.B., Greig, L.C., Liu, K.X., Ippolito, G.C., Tucker, H.O., and Macklis, J.D. (2016). Ctip1 Regulates the Balance between Specification of Distinct Projection Neuron Subtypes in Deep Cortical Layers. Cell Rep. *15*, 999–1012.

84. Hatten, M.E. (1999). Central nervous system neuronal migration. Annu. Rev. Neurosci. *22*, 511–539.

85. Rakic, P. (1988). Defects of neuronal migration and the pathogenesis of cortical malformations. Prog. Brain Res. *73*, 15–37.

86. Andrews, M.G., Subramanian, L., and Kriegstein, A.R. (2020). mTOR signaling regulates the morphology and migration of outer radial glia in developing human cortex. Elife *9*, e58737.

87. Tabata, H., Kanatani, S., and Nakajima, K. (2009). Differences of migratory behavior between direct progeny of apical progenitors and basal progenitors in the developing cerebral cortex. Cereb. Cortex *19*, 2092–2105.

88. Steinecke, A., Gampe, C., Nitzsche, F., and Bolz, J. (2014). DISC1 knockdown impairs the tangential migration of cortical interneurons by affecting the actin cytoskeleton. Front. Cell. Neurosci. *8*, 190.

89. John, J.P., Thirunavukkarasu, P., Ishizuka, K., Parekh, P., and Sawa, A. (2019). An in-silico approach for discovery of microRNA-TF regulation of DISC1 interactome mediating neuronal migration. NPJ Syst. Biol. Appl. *5*, 17.

90. Enomoto, A., Asai, N., Namba, T., Wang, Y., Kato, T., Tanaka, M., Tatsumi, H., Taya, S., Tsuboi, D., Kuroda, K., et al. (2009). Roles of disrupted-in-schizophrenia 1-interacting protein girdin in postnatal development of the dentate gyrus. Neuron *63*, 774–787.

91. Chen, X., Ku, L., Mei, R., Liu, G., Xu, C., Wen, Z., Zhao, X., Wang, F., Xiao, L., and Feng, Y. (2017). Novel schizophrenia risk factor pathways regulate FEZ1 to advance oligodendroglia development. Transl. Psychiatry *7*, 1293.

92. Schindelin, J., Arganda-Carreras, I., Frise, E., Kaynig, V., Longair, M., Pietzsch, T., Preibisch, S., Rueden, C., Saalfeld, S., Schmid, B., et al. (2012). Fiji: an open-source platform for biological-image analysis. Nat. Methods *9*, 676–682.

93. Pei, Y., Sierra, G., Sivapatham, R., Swistowski, A., Rao, M.S., and Zeng, X. (2015). A platform for rapid generation of single and multiplexed reporters in human iPSC lines. Sci. Rep. *5*, 9205.

94. An, O., Tan, K.T., Li, Y., Li, J., Wu, C.S., Zhang, B., Chen, L., and Yang, H. (2020). CSI NGS portal: An online platform for automated NGS data analysis and sharing. Int. J. Mol. Sci. *21*, 3828.

95. Dobin, A., Davis, C.A., Schlesinger, F., Drenkow, J., Zaleski, C., Jha, S., Batut, P., Chaisson, M., and Gingeras, T.R. (2013). STAR: ultrafast universal RNA-seq aligner. Bioinformatics *29*, 15–21.

96. Anders, S., Pyl, P.T., and Huber, W. (2015). HTSeq–a Python framework to work with high-throughput sequencing data. Bioinformatics *31*, 166–169.

97. Love, M.I., Huber, W., and Anders, S. (2014). Moderated estimation of fold change and dispersion for RNA-seq data with DESeq2. Genome Biol. *15*, 550.

98. Zhou, Y., Zhou, B., Pache, L., Chang, M., Khodabakhshi, A.H., Tanaseichuk, O., Benner, C., and Chanda, S.K. (2019). Metascape provides a biologist-oriented resource for the analysis of systems-level datasets. Nat. Commun. *10*, 1523.

99. Butler, A., Hoffman, P., Smibert, P., Papalexi, E., and Satija, R. (2018). Integrating single-cell transcriptomic data across different conditions, technologies, and species. Nat. Biotechnol. *36*, 411–420.

100. Hafemeister, C., and Satija, R. (2019). Normalization and variance stabilization of single-cell RNA-seq data using regularized negative binomial regression. Genome Biol. *20*, 296.

101. Raudvere, U., Kolberg, L., Kuzmin, I., Arak, T., Adler, P., Peterson, H., and Vilo, J. (2019). g:Profiler: a web server for functional enrichment analysis and conversions of gene lists (2019 update). Nucleic Acids Res. *47*, W191–W198.

102. Kostović, I. (2020). The enigmatic fetal subplate compartment forms an early tangential cortical nexus and provides the framework for construction of cortical connectivity. Prog. Neurobiol. *194*, 101883.

STAR★METHODS

KEY RESOURCES TABLE

REAGENT or RESOURCE	SOURCE	IDENTIFIER
Antibodies		
Rabbit anti-Neural Cell Adhesion Molecule (NCAM)(1:120)	Merck	Cat#AB5032, RRID:AB_2291692
Rabbit anti-TUJ1 (β3-Tubulin) (1:300)	Synaptic Systems	Cat#302302, RRID:AB_10637424
Guinea Pig anti-TUJ1 (β3-Tubulin) (1:300)	Synaptic Systems	Cat#302304, RRID:AB_10805138
Rat anti-Ctip2 (1:500)	Abcam	Cat#ab18465, RRID:AB_2064130
Rabbit anti-Fez1 (IF: 1:400; WB: 1:1000)	In house	clone361
Rabbit anti-GAPDH (WB: 1:1000)	Abcam	Cat#ab9485, RRID:AB_307275
Alexa Fluor™ 647 Phalloidin (1:500) (F-actin)	Thermo Fisher Scientific	Cat#A22287, RRID:AB_2620155
Deoxyribonuclease I, Alexa Fluor™ 488 Conjugate (1:500) (G-actin)	Thermo Fisher Scientific	Cat#D12371
Guinea pig anti-Doublecortin (DCX) (1:600)	Merck	Cat#AB2253, RRID:AB_1586992
DAPI (4′,6-Diamidino-2-Phenylindole, Dihydrochloride)	Thermo Fisher Scientific	Cat#D1306, RRID:AB_2629482
Mouse anti-N cadherin (1:100)	Abcam	Cat#ab19348, RRID:AB_444868
Rabbit anti-E-cadherin (IF: 1:50)	Santa Cruz	Cat#sc-7870, RRID:AB_2076666
Rabbit anti-Nestin (1:200)	Abcam	Cat#ab92391, RRID:AB_10561437
Sheep anti-Pax6 (1:50)	R&D Systems	Cat#AF8150, RRID:AB_2827378
Mouse anti-Lin28a (6D1F9) (IF 1:1000)	Cell Signaling	Cat#5930S, RRID:AB_1903976
Rabbit anti-Nanog (IF: 1:500)	Cell Signaling	Cat#3580S, RRID:AB_2150399
Mouse anti-SSEA4 (IF: 1:500)	Abcam	Cat#ab16287, RRID:AB_778073
Mouse anti-Phosphorylated Vimentin (1:250)	MBL	Cat#D076-3, RRID:AB_592963
Mouse anti-SOX2 (1:300)	R&D Systems	Cat#MAB2018, RRID:AB_358009
Rabbit anti-TBR2 (1:300)	Abcam	Cat#ab23345, RRID:AB_778267
Mouse anti-Ki 67 (1:100)	BD Transduction Laboratories™	Cat#610969, RRID:AB_398282
Rabbit anti-QKI (IF: 1:100)	Abcam	Cat#ab126742, RRID:AB_11129508
Rabbit MOXD1 (IF: 1:150)	Sigma-Aldrich	Cat#HPA035740, RRID:AB_10610141
Donkey anti-Mouse IgG (H + L) Highly Cross-Adsorbed Secondary Antibody, Alexa Fluor Plus 488 (1:500)	Thermo Fisher Scientific	Cat#A32766, RRID:AB_2762823
Donkey anti-Sheep IgG (H + L) Cross-Adsorbed Secondary Antibody, Alexa Fluor 555 (1:500)	Thermo Fisher Scientific	Cat#A-21436, RRID:AB_2535857
Goat anti-Guinea Pig IgG (H + L) Highly Cross-Adsorbed Secondary Antibody, Alexa Fluor 555 (1:500)	Thermo Fisher Scientific	Cat#A-21435, RRID:AB_2535856
Donkey anti-Rabbit IgG (H + L) Highly Cross-Adsorbed Secondary Antibody, Alexa Fluor Plus 647 (1:500)	Thermo Fisher Scientific	Cat#A32795, RRID:AB_2762835
Goat anti-Mouse IgG (H + L)-HRP Conjugate (1:4000)	Bio-Rad	Cat#170–6516, RRID:AB_11125547
Goat anti-Rabbit IgG (H + L)-HRP Conjugate (1:4000)	Bio-Rad	Cat#170–6515, RRID:AB_11125142
Donkey anti-Rat IgG (H + L)(Cy2) (1:200)	Jackson ImmunoResearch	Cat#712-225-150, RRID: AB_2340673
Donkey Anti-Guinea Pig IgG (H + L) (Cy2) (1:200)	Jackson ImmunoResearch	Cat#706-225-148, RRID: AB_2340467
Donkey Anti-Sheep IgG (H + L) (Cy5) (1:200)	Jackson ImmunoResearch	Cat#713-175-147, RRID: AB_2340730

Continued

REAGENT or RESOURCE	SOURCE	IDENTIFIER
Bacterial and virus strains		
Lentivirus (pLenti-CRISPR-FEZ1-KO)	In-house	N.A.
AAV (EF1a/CMV-GFP)	Gift from Dr.Ayumu Tashiro (Nanyang Technological University)	N.A.
Chemicals, peptides, and recombinant proteins		
Matrigel® hESC-Qualified Matrix, LDEV-free	Corning	Cat#354277
TRIzol™ Reagent	Thermo Fisher Scientific	Cat#15596026
Pierce™ 16% Formaldehyde (w/v), Methanol-free	Thermo Fisher Scientific	Cat#28908
Matrigel® Growth Factor Reduced (GFR) Basement Membrane Matrix, LDEV-free	Corning	Cat#354230
N-2 Supplement (100X)	Thermo Fisher Scientific	Cat#17502048
B-27™ Supplement	Thermo Fisher Scientific	Cat#17504044
Y-27632	STEMCELL Technologies	Cat#72304
Puromycin	Merck	Cat#P8833-10MG, CAS number: 58-58-2
Critical commercial assays		
CloneR™	STEMCELL Technologies	Cat#05888
CellTiter 96® AQueous One Solution Cell Proliferation Assay (MTS)	Promega	Cat#G3582
CyQUANT™ XTT Cell Viability Assay	Thermo Fisher Scientific	Cat#X12223
RapiClear 1.52	SunJin Lab Co.	Cat#RC152001
Taq PCR Core Kit	Qiagen	Cat#201223
Wizard(R) Genomic DNA Purification Kit	Promega	Cat#A1120
PowerUp™ SYBR™ Green Master Mix	Thermo Fisher Scientific	Cat#A25742
STEMdiff™ Cerebral Organoid Kit	STEMCELL Technologies	Cat#08570
Click-iT™ Plus EdU Alexa Fluor™ 555 Imaging Kit	Thermo Fisher Scientific	Cat#C10638
RNeasy Mini Kit	Qiagen	Cat#74106
SensiFAST™cDNA synthesis kit	Bioline	Cat#BIO-65054
Deposited data		
RNAseq and scRNAseq datasets	Gene Expression Omnibus (GEO)	GSE218845, GSE214538
Experimental models: Cell lines		
H1 hESC line	WiCell, Madison, WI	Cat#WA01
hiPSC-DCX (AAVS-DCX-GFP)	XCell Science	Cat#IP-001-ZIX4-1V
Oligonucleotides		
Primers for RT-PCR: human Fez1: forward 5′-ACTACAA CGCCAAGACC-3′ and reverse 5′-AGAGCATCCCAAACCT-3′; human Gapdh: forward 5′-TGCACCACCAACTGCTTAGC-3′ and reverse 5′ GGCATGGACTGTGGTCATGAG	Integrated DNA Technologies (IDT)	N.A.
Primers for PCR: human Fez1: forward 5′-ATAAACTCAT CCTGAAAGTCGCTG-3′ and reverse 5′-CCTCGTCCTG AAGGGTCTCCT-3′	Integrated DNA Technologies (IDT)	N.A.
Software and algorithms		
ImageJ/Fiji	Schindelin et al.[92]	https://imagej.nih.gov/ij/download.html RRID:SCR_003070/RRID:SCR_002285
ZEN lite	Zeiss	https://www.zeiss.com/microscopy/int/downloads.html RRID:SCR_013672

Continued

REAGENT or RESOURCE	SOURCE	IDENTIFIER
Imaris 9.5.1	Oxford Instruments	http://www.bitplane.com/imaris/imaris RRID:SCR_007370
BioTuring Browser	BioTuring	https://bioturing.com/bbrowser
Partek Flow	Partek	https://www.partek.com/partek-flow/

RESOURCE AVAILABILITY

Lead contact

Further information and requests for resources and reagents should be directed to and will be fulfilled by the lead contact: Dr John Jia En Chua (phsjcje@nus.edu.sg).

Materials availability

Plasmids and cell lines generated in this paper will be shared by the lead contact upon request.

Data and code availability

- This paper does not report original code.
- RNAseq and scRNAseq data have been deposited at Gene Expression Omnibus and are publicly available as of the date of publication. Accession numbers are listed in the key resources table.
- Any additional information required to reanalyze the data reported in this paper is available from the lead contact upon request.

EXPERIMENTAL MODEL AND STUDY PARTICIPANT DETAILS

Human ESC line and iPSC line (hPSC lines)

All human stem cell work was performed with approval from National University of Singapore (NUS). hiPSC-DCX (AAVS-DCX-GFP) line was characterized and provided by Prof Zeng Xianmin in kind.[93] The hESC line H1 (WiCell, Madison, WI) and hiPSC-DCX (both derived from a male donor) were maintained in *Mycoplasma* free conditions with routine *Mycoplasma* test every six months. Feeder free hPSC lines were maintained on hESC qualified Matrigel coated cell culture plate in mTeSR™1 (STEMCELL Technologies, Cat#85850), passaged with ReLeSR™ (STEMCELL Technologies, Cat# 05872) or Gentle Cell Dissociation Reagent (STEMCELL Technologies, Cat#100-0485) and frozen in CryoStor® CS10 (STEMCELL Technologies, Cat#07930) according to the manufacturer's recommendations.

METHOD DETAILS

Generation of FEZ1 knockout (KO) hPSC lines by CRISPR/CAS9

Design of sgRNA, construction and production of lentiviruses have been previously described.[14,16] Briefly, gRNA sequence targeting exon 2 of human *FEZ1* gene (forward 5'-AATCAGCTTCAAGTCCATGG-3' and reverse 5'-CCATGGACTTGAAGCTGATT-3') were designed using the online CRISPR design tool (http://crispr.mit.edu/) and inserted into LentiCRISPRv2 plasmid (Addgene, plasmid #52961). pLenti-CRISPR-FEZ1-KO vector was co-transfected with pMDLg/pRRE (Addgene; plasmid #12251), pRSV-rev (Addgene; plasmid #12253) and pMD2.G helper plasmids (Addgene; plasmid #12259) (2:1:1) into HEK293. Cell supernatant containing lentiviruses was collected after 24 h of post-transfection and concentrated with Amicon Ultra-15 filters (Millipore) by ultracentrifugation at 3,220× *g* for 30 min at 4°C.

To generate FEZ1 KO hPSCs, cells at 60% to 70% confluence one day after seeding on 12-well plates were infected with 100 μL of concentrated lentiviruses and cultured in mTeSR™1 for 24 hours. Twenty-four hours post infection, successfully transduced cells were selected using 5 μg/ml (H1) or 2 μg/ml (iPSC-DCX) puromycin for 24 to 48 h. Positively selected cells were then dissociated with Accutase (ThermoFisher Scientific, Cat#A1110501) and passed through 40 μM cell strainer (Fisher scientific, Falcon, Cat#352340). Single cells obtained were plated at a density of 1,500 cells on a 10-cm dish coated with hESC qualified Matrigel. Cells were maintained in mTeSR™1 supplemented with CloneR™ (STEMCELL Technologies) for the first 3 days of culture followed by mTeSR™1 maintenance culture for another 5 to 8 days until individual colonies reached a diameter larger than 1 mm. After a 3-minute treatment with Dispase (STEMCELL Technologies, Cat#07923), distinct colonies were individually picked up under an inverted microscope and carefully transferred into individual wells of 24-well plate. Colonies that are fused or close-by one another are avoided. The selected clones were then expanded and stored to generate clonal banks of FEZ1 KO hPSCs for further characterization and application. Karyotyping for selected FEZ1 KO hPSCs was performed by the KK Women's and Children's Hospital (Singapore). Cell proliferation was measured using the CyQuant kit (ThermoFisher Scientific, Cat#X12223) according to the manufacturer's recommendations.

Genomic sequencing of FEZ1 knockout (KO) hPSC lines

To confirm the successful generation of FEZ1 KO hPSC lines, selected clones from FEZ1-null hPSCs bank were expanded and cell DNA were extracted and purified with Wizard® Genomic DNA Purification Kit (Promega, Cat#A1120). DNA amplification prior to sequence was performed by Taq PCR Core Kit (Qiagen, Cat#201223) and FEZ1 primers targeting the editing site (forward 5′-ATAAACTCATCCT GAAAGTCGCTG-3′ and reverse 5′-CCTCGTCCTGAAGGGTCTCCT-3′). Amplicons were analyzed by sequencing (forward 5′-AATCAGCTT CAAGTCCATGG-3′ and reverse 5′-CCATGGACTTGAAGCTGATT-3′) and results were analyzed with FinchTV and BLAST® (https://blast.ncbi.nlm.nih.gov/Blast.cgi) to characterize the nature of the indels in hPSCs.

2D neural epithelium (NE) induction

To differentiate NE on monolayer culture, hPSCs were dissociated with Accutase (ThermoFisher Scientific, Cat#A1110501) and plated on hESC qualified Matrigel (Corning, Cat#354277)-coated 6-well cell culture plates at a density of 0.1 million cells/cm^2. Cells were maintained in freshly prepared N2B27 medium (50 ml of Neurobasal medium (ThermoFisher Scientific, Cat#21103049), 50 ml of DMEM/F12 Glutmax (ThermoFisher Scientific, Cat#10565018), 0.1 mM of b-mercaptoethanol (ThermoFisher Scientific, Cat#21985023), 0.2 mM of glutamine (ThermoFisher Scientific, Cat#25030081), 0.5× N2 supplement (ThermoFisher Scientific, Cat#17502048) and 0.5× B27 supplement (ThermoFisher Scientific, Cat#17504044) to obtain 100 ml N2B27 medium) with daily change of medium for 6 days as previously described.[36] After 6 days of NE induction, the cells were harvested based on the requirements for various downstream assays. For each assay, at least three independent experiments were performed.

Generation of human cerebral organoids (hCOs)

hCOs were generated by using the STEMdiff™ Cerebral Organoid Kit (STEMCELL Technologies, Cat#08570), which consisted of Embryoid body (EB) formation media, induction medium, expansion medium and organoid maturation medium. Freshly thawed hPSC were maintained in mTeSR™1 until 70-80% confluency and then dissociated with Accutase to obtain single cells. EB were generated by seeding 9,000 viable cells/well in a 96-well round bottom ultra-low attachment microplate (Corning, Cat. 7007) in EB formation media supplemented with ROCKi/Y-27632 (STEMCELL Technologies, Cat#72304). After 5 days, EBs were transferred to individual wells containing induction medium in 48-well suspension culture plates (Greiner, Cat. 677102) and grown for 2 days. At day 7, each EB was embedded in Matrigel (Corning, growth factor reduced basement membrane matrix, Cat#354230) and transferred into a 6-well suspension culture plate (Greiner, Cat#657185) containing expansion medium. At day 10, expansion medium was removed from hCOs and replaced with organoid maturation medium. The culture plates containing the hCOs were then placed onto an orbital shaker (Stuart, Cat# SSM1) in a 37°C incubator with gentle agitation at 80 rpm to allow hCOs to develop in organoid maturation medium with medium change every 3 or 4 days. Organoid morphologies were routinely monitored by microscopy (Nikon, Eclipse TS100 equipped DS-Fi1/Digital sight DS-L2 camera and Nikon, Eclipse TE2000-E). For each downstream assay, at least 3 or 4 biological repeats of organoids were used.

Immunofluorescence (IF) microscopy

For monolayer cell cultures, cells were fixed with 4% formaldehyde (by diluting the 16% formaldehyde (ThermoFisher Scientific, Cat#28908) with 1xPBS) for 20 mins at room temperature and then washed with calcium-free phosphate-buffered saline (1×PBS, 1st BASE, Cat#BUF-2040-1X500 ml, containing 137 mM sodium chloride, 2.7 mM potassium Chloride and 12 mM phosphate buffer). Permeabilization was performed using 0.4% Triton X-100 (Sigma-Aldrich, Cat#X100-500ML) in 1×PBS for 20 minutes. After washing, cells were blocked in blocking buffer (2% BSA, 0.2% Triton X-100 in 1×PBS) for 1 hour. Incubation with primary antibodies were performed overnight at 4°C. After washing, samples were incubated with secondary antibodies at room temperature for 2 hours. After washing, samples were mounted with FluorSave™ (Merck, Cat#345789) for epifluorescence (Nikon, Eclipse Ti2; Zeiss, Axio Observer Z1 and Nikon, Eclipse TE2000-E) or confocal (Zeiss LSM800) imaging. For each assay, at least 3 independent experiments were performed.

Whole hCOs were fixed with 4% FA for 2 hours (D10 and D28 hBOs) or 3 hours (hCOs older than 28 days) at room temperature. Organoids were then washed with 1× PBS to remove any remaining FA. Fixed hCOs were either stored in 1× PBS at 4°C or permeabilized for 2 days (1% Triton X-100 and 1% DMSO in 1×PBS) and blocked for an additional 2 days (2% BSA, 1% Triton X-100, 1% DMSO and 1% sodium azide in 1× PBS). After blocking, organoids were then incubated with primary antibodies diluted in antibody dilution buffer (2% BSA, 0.2 % Triton X-100, 1% DMSO, 1% sodium azide, and 1% Heparin in 1× PBS) for 2 to 3 days depending on the age of the hCOs. Samples were then washed thrice with washing buffer (3% NaCl and 0.2% Triton X-100 in 1× PBS) for at least 12 hours. hCOs were then incubated with secondary antibodies and DAPI in antibody dilution buffer for 2 to 3 days and washed as before. After the final washing step, hCOs were rinsed once with 1× PBS and left in 1× PBS for at least 6 hours to remove any remaining Triton X-100. hCOs were then cleared overnight with RapiClear 1.52 (Sunjin Lab, Cat#RC152001) and mounted on iSpacer (Sunjin Lab, 0.5 mm, Cat#IS008). Scanning of cleared hBOs was performed on Zeiss LSM800 confocal microscopy equipped with a long working distance (0.57 mm) multi-immersion objective lens (Zeiss, Objective LD LCI Plan-Apochromat 25x/0.8 Imm Corr DIC M27). For each assay, at least 3 independent experiments were performed.

Antibodies used for IF labeling are as follows: Primary antibodies: Sheep anti-Pax6 (1:50, R&D Systems, Cat#AF8150); Mouse anti-N cadherin (1:100, Abcam, Cat#ab19348); Mouse anti-Phosphorylated Vimentin (1:250, MBL, Cat#D076-3); Rabbit anti-Nestin (1:200, Abcam, Cat#ab92391); Rabbit anti-TUJ1 (1:300, Synaptic Systems, Cat#302302); Guinea Pig anti-TUJ1 (1:300, Synaptic Systems, Cat#302304); Rat anti-Ctip2 (1:500, Abcam, Cat#ab18465); Guinea pig anti-DCX (1:600, Merck, Cat#AB2253); Rabbit anti-TBR2 (1:300, Abcam, Cat#ab23344);

Mouse anti-Ki 67 (1:100, BD Transduction Laboratories™, Cat#610969); Rabbit anti-NCAM (1:120, Merck, Cat#AB5032); Rabbit anti-QKI (1:100, Abcam, Cat#ab126742). Secondary antibodies: Donkey anti-Mouse IgG (H+L) Highly Cross-Adsorbed Secondary Antibody, Alexa Fluor Plus 488 (1:500, Thermo Fisher Scientific, Cat#A32766); Donkey anti-Sheep IgG (H+L) Cross-Adsorbed Secondary Antibody, Alexa Fluor 555 (1:500, Thermo Fisher Scientific, Cat#A-21436); Donkey anti-Rabbit IgG (H+L) Highly Cross-Adsorbed Secondary Antibody, Alexa Fluor Plus 647 (1:500, Thermo Fisher Scientific, Cat#A32795); Goat anti-Guinea Pig IgG (H+L) Highly Cross-Adsorbed Secondary Antibody, Alexa Fluor 555 (1:500, Thermo Fisher Scientific, Cat#A-21435); Donkey anti-Rat IgG (H+L)(Cy2) (1:200, Jackson ImmunoResearch, Cat#712-225-150). VZ-like regions were defined by PAX6$^+$ regions that are devoid of TUJ1$^+$, TBR2$^+$, DCX$^+$, CTIP2$^+$ and etc. SVZ-like regions were defined by TBR2$^+$ cells while PP-like regions were defined by CTIP2$^+$ region.

EdU labeling

EdU assay was performed using the Click-iT® Plus EdU Alexa Fluor™ 555 Imaging Kit (ThermoFisher Scientific, Cat#C10638). Day 23 hCOs were first incubated with 5 μM EdU in maturation medium with continuous agitation. After 4 hours of incubation, EdU medium was removed and replaced with fresh maturation medium after rinsing twice with DMEM/F-12 (ThermoFisher Scientific, Cat#11330107). EdU-labeled hCOs were then fixed at day 28 with 4% PFA for 2 h at room temperature. Immediately after fixation, permeabilization and blocking were performed as described in the preceding section. After blocking, EdU-labelled hCOs were incubated overnight at room temperature protected from light with Click-iT® Plus reaction cocktail containing 1X Click-iT® reaction buffer, copper protectant, Alexa Fluor® picolyl azide and reaction buffer additive. After washing, hCOs were incubated again in blocking buffer overnight followed by primary and secondary antibody staining steps (details can be found under section on "immunofluorescence (IF) microscopy") for hCOs to co-stain EdU with other antibodies. Antibodies used for co-staining with BrdU were as follows: Primary antibodies: Sheep anti-Pax6 (1:50, R&D Systems, Cat#AF8150); Guinea Pig anti-TUJ1 (1:300, Synaptic Systems, Cat#302304). Secondary antibodies: Donkey Anti-Guinea Pig IgG (H+L) (Cy2) (1:200, Jackson ImmunoResearch, Cat#706-225-148) and Donkey Anti-Sheep IgG (H+L) (Cy5) (1:200, Jackson ImmunoResearch, Cat#713-175-147). Four independent experiments were performed and analyzed for D28 BrdU assays.

Protein sample preparation and immunoblot assays

For monolayer cell cultures, cells were lysed with HEPES lysis buffer (50 mM HEPES, 150 mM NaCl, 1 mM EDTA, 1% Triton X-100, pH 7.2) as described previously.[9] In brief, cells were washed once with cold 1xPBS and subsequently incubated with cold HEPES buffer on rocker for 10 minutes at 4°C. Cell lysates were collected and centrifuged at 10,000× g for 10 minutes at 4°C. Supernatant was collected and mixed with 4×NuPAGE LDS Sample Buffer (ThermoFisher Scientific, Cat#NP0008) for immunoblot analyses or stored at -20°C.

For organoid samples, hCOs were homogenized in sucrose buffer (320 mM sucrose, 1 mM EDTA, 5 mM HEPES, pH 7.4) with homogenizer (Bandelin, Sonopuls ultrasonic homogenizer) to obtain the homogenized cell lysate. Homogenates were centrifuged at 2,000× g for 2 minutes to separate nuclei (pellet) from cell lysate (Pavlos et al., 2010). The S1 supernatants were then centrifuged again at 14,500× g for 12 minutes. The S2 supernatant were then harvested and mixed with 4×NuPAGE LDS Sample Buffer for immunoblot analyses or stored at -80°C.

To perform immunoblot analysis, protein samples were resolved by SDS-PAGE and transferred onto nitrocellulose membranes (Bio-Rad) using the Trans-Blot Turbo Transfer System (Bio-Rad). Membranes were then blocked with 5% skim milk in TBST (1.5 M NaCl, 0.5% Tween 20, 150 mM Tris-HCl, pH 7.4) and subsequently incubated with primary antibodies at 4°C overnight. After three washes with TBST, the membranes were then incubated with secondary antibodies for 1 hour at room temperature. After washing, membranes were treated with Immobilon Forte Western HRP Substrate (Millipore, Cat#WBLUF0500). Protein bands were visualized and captured by Azure Biosystem C300 (Azure Biosystems). Quantification of immunoblot was performed with ImageJ/Fiji and the intensities normalized against GAPDH. At least 3 independent batches of protein samples were used to run the immunoblot assay and quantification.

Antibodies used for immunoblot assays are as follows: Primary antibodies: Rabbit anti-Fez1 (IF: 1:1000); Rabbit anti-GAPDH (WB: 1:1000, Abcam, Cat#ab9485). Secondary antibodies: Goat anti-Rabbit IgG (H + L)-HRP Conjugate (1:4000, Bio-Rad, Cat#170-6515).

Cell migration studies in hCOs

To observe cell migration in unfixed hCOs, 5 days-old hCOs were transferred to cell culture imaging dishes (ibidi, Cat#81156) in induction medium. On day 6, hCOs were infected with GFP-expressing AAVs (a kind gift from Dr Ayumu Tashiro) for 24 hours in induction medium. Live imaging was carried out by confocal microscopy on a Zeiss LSM800 with the temperature of the imaging chamber set at 37°C. For imaging, organoid maturation medium was supplemented with 25 mM HEPES to maintain pH. Images for the GFP and differential interference contrast channels were acquired at a rate of 1 frame every 20 minutes over a 20-hour recording period. At least 10 different locations were chosen for analyses per hCO. 3 independent experiments were performed for each group of hCOs for live imaging. Image stacks were processed and analyzed using Imaris 9.5.1(Bitplane). The details of quantification are described in the section on "quantification of IF images".

Bulk RNA sequence (RNA-seq) sample preparation and RT-PCR

Cells or hCOs were lysed with the TRIzol™ reagent (ThermoFisher Scientific, Cat#15596026). The lysates were then mixed with chloroform and centrifuged at 16,200× g for 15 minutes at 4°C. The top colorless layer was carefully aspirated, mixed with 70% ethanol and loaded into RNeasy spin columns (Qiagen, RNeasy Mini Kit, Cat#74106) to obtain purified mRNA.

For bulk RNA sequence, a pre-quality check was done by agarose electrophoresis to check the quality of the 18S and 28S ribosomal RNAs. Samples were then processed by Novagene (Singapore) for additional QC, library preparation and total RNA-seq using an Illumina NovaSeq 6000 platform to obtain a sequencing depth of 20 million read pairs per sample. Data were acquired from 3 independent batches of samples with a total of 4 repeats for both WT and FEZ1-null groups. Data were acquired from 40 organoids for each genotype of WT and FEZ1-null, across 3 independent differentiations of organoids.

For RT-qPCR assays, 1 μg of mRNA was converted to cDNA using the SensiFAST™ cDNA synthesis kit (Bioline, Cat#BIO-65054). 10 ng of cDNA were used for PCR amplification of each targeted gene using the PowerUp™ SYBR™ Green Master Mix (ThermoFisher Scientific, Cat#A25742). RT-qPCR quantification was performed on QuantStudio 3 Real-Time PCR System (ThermoFisher Scientific). Primers used in RT-PCR study were as follows: human *Fez1*: forward 5′-ACTACAACGCCAAGACC-3′ and reverse 5′-AGAGCATCCCAAACCT-3′; human *Gapdh*: forward 5′-TGCACCACCAACTGCTTAGC-3′ and reverse 5′ GGCATGGACTGTGGTCATGAG-3′. The expression levels of genes were normalized against *Gapdh*. Transcript levels from differentiated samples were compared against undifferentiated cells to obtain fold change. Repeats were conducted with 3 independent batches of samples.

Single-cell RNA sequencing (scRNA-seq)

We modified our in-house rat hippocampal cell isolation protocol to obtain single-cell samples for scRNA-seq.[14] hCOs were dissected into smaller pieces by scalpel and trypsinized by Trypsin/EDTA solution (Lonza, Cat#CC-5012) for 25 min. Digestion was stopped by adding serum medium (Modified Eagle's Medium (Sigma-Aldrich, Cat#M2414-500ML) supplemented with 5% fetal calf serum (Biochrom, Cat#50115), 2 mM L-alanyl-L-glutamine (Biochrom, Cat#K0302), 1× MEM Vitamin Solution (Biochrom, Cat#K0373), 0.2x Mito+Serum extender (BD, Cat#355006) and 21 mM D-glucose (Merck, Cat#1.08337.1000). The fragments were then gently triturated with a Pasteur pipette and the suspension spun down at 500× g for 5 min. Pelleted cells were resuspended in ESCAPE™ buffer (provided by Proteona) and passed through a 40 μm strainer. Cell viability and counts were determined (viability > 85% and cell count > 1 million/sample). Single cell sample library preparation and sequencing were done by Proteona (Singapore). Only QC passed single alive cells were used for library preparation using the 3′RNA V3 kit on 10× Genomics Chromium Controller. Cell suspensions were processed with the Chromium Controller (10x Genomics) using Chromium Single Cell 3′ Gem, Library & Gel Bead Kit v3 (10x Genomics, Cat# PN-1000078) and Chromium Single Cell B Chip Kit (10x Genomics, Cat# PN-1000074). RNA libraries that met QC criteria were sent for further sequencing using HiSeq X (Illumina) with 150 bp paired end reads.

Bulk RNA-seq analysis

The raw RNA-seq data was uploaded to NUS Cancer Science Institute of Singapore (CSI) NGS Portal (https://csibioinfo.nus.edu.sg/csingsportal)[94] to perform gene expression profiling and differential expression analysis. Briefly, clean reads were aligned to the reference human genome (hg19) with default parameters.[95] The gene expression quantification was done by using HTSeq-count in strand-specific mode with "-s reverse" option and read counts only from the sense strand were used for each gene.[96] Differential gene expression analysis was performed by using DESeq2.[97] The genes that did not express or in low expression (read counts less than 2 on average per sample) were removed from the analysis. After correction for multiple hypothesis testing (adjusted p value (Padj) < 0.05, using Benjamini-Hochberg method), 87 and 439 genes were identified with significant up- and downregulation in the FEZ1-null group when compared to WT group. We further narrowed down the significant expressed genes by applying expression fold change (log2 KO/WT) cut off at +/- 1 as differentially expressed genes (DEGs, 42 and 383 genes were identified with significant up- and downregulation in the FEZ1-null group when compared to WT group) for the subsequent analysis, including Gene Ontology (GO) and pathway enrichment analysis by Metascape[98] and disease related gene enrichment analysis by Enrichr (https://maayanlab.cloud/Enrichr/).

scRNA-seq analysis

The Cell Ranger 3.1.0 pipeline (10x Genomics) was used to align reads from scRNA-seq to the GRCh38 human reference genome and the associated gene by cell count matrix was generated. The default parameters were used except for specifying the expected number of cells ('−expect-cells=10000'). The resulting matrices containing the unique molecular identifier (UMI) counts were merged from WT and FEZ1-null samples into a single object and analyzed by the Seurat R package v.3.1.[99] Cells expressing a range of 1000-8000 genes and less than 20% of mitochondrial genes were retained based on the inspection of feature distributions, and genes expressed in less than 10 cells were filtered out. UMI counts were normalized and variance-stabilized by using 'SCTransform' function which employs a regularized negative binomial regression to remove technical differences between cells due to sequencing depth.[100] This step was accompanied by regressing out variation due to proportion of mitochondrial gene expression and identifying top 3000 most variable genes. Principal component analysis (PCA) was performed on the normalized data for the variable genes, and the first 30 principal components were used for clustering. In this PCA space, the cells were clustered by finding the nearest 20 neighbors to each cell (FindNeighbors function with 'dims=1:30'), building a Shared Nearest Neighbor (SNN) graph with edges between neighbor cells weighted by the Jaccard index, and performing Louvain algorithm on the resulting graph (FindClusters function with 'resolution=0.8'). The clusters of cells were then visualized in two-dimensional space by using t-distributed Stochastic Neighbor Embedding (t-SNE) projection. The resulting 26 clusters were manually merged into 14 clusters and assigned to corresponding cell types based on the expression of known marker genes: vNE/vRG (ventricular neuroepithelium/ radial glia cells): *LIX1, NES, HMGA2, PAX6*; Dividing vNE/vRG: *MKI67, LIX1, PAX6, ASPM*; tRG (truncated radial glia cells): *CRYAB, EGR1, HMGA2*; HOPX- oRG (HOPX- outer radial glia cells): *FABP7, MOXD1, QKI, CLU*; HOPX+ oRG (HOPX+ outer radial glia cells): *FABP7, CLU, FEZF2, HOPX*; Dividing

oRG: *MIK67, HJURP, FABP7, CLU, FEZF2, HOPX*; CP (choroid plexus): *TTR, OTX2*; IP (intermediate progenitor): *EOMES, DCX, BEUROG1*; Dividing IP: *EOMES, MKI67, BEUROG1*; New born neuron: *STMN2, DCX*; Deep layer neuron: *STMN2, NEUROD6, BCL11B*; Upper layer neuron: *POU3F2, BHLHE22*; Interneuron: *DLX5, GAD2, DLX1*; Pericyte: *COL3A1, LUM*.

For each sample (WT and FEZ1-null), differentially expressed genes (DEGs) that were upregulated or downregulated in each cluster compared to the rest of the cells were identified and visualized by using Partek Flow (https://www.partek.com/partek-flow/) and Bioturing (https://bioturing.com/) (DEG filtering: false discovery rate (FDR)<0.01, log$_2$FC>0.137 or <-0.137).[60] Gene Ontology (GO) and pathway enrichment analysis of DEG in specific clusters were visualized by Metascape,[98] DAVID and g:Profiler (version e99_eg46_p14_f929183) with g:SCS multiple testing correction method, applying a significance threshold of 0.05.[101] The trajectory analysis was perform using Patek Flow. In brief, maker genes (known as DEGs) from vNE/vRG, HOPX- oRG and HOPX+ oRG clusters (Table S4) were used as feature genes to generate the trajectory plot for both WT and FEZ1-null groups. Pseudotime plot was subsequently calculated and generated from the trajectory analysis by Patek Flow as well.

F-actin and G-actin assays

F-actin and G-actin measurement was performed as described.[65] D28 hCOs were dissociated into single cells using the same method used for scRNA-seq. Harvested cells were resuspended in organoid maturation medium and passed through a 40 μm filter strainer to obtain single cells. Cells then seeded at a density of 0.05 million/well on 24-well size coverslips coated with hESC qualified Matrigel. After two days in culture, cells were fixed with 4% PFA for 15 min. Permeabilization and blocking of the samples are performed as mentioned in the section on immunofluorescence microscopy. After blocking, cells were stained with antibody Alexa Fluor™ 647 Phalloidin (F-actin, ThermoFisher Scientific, Cat#A22287), Deoxyribonuclease I, Alexa Fluor™ 488 Conjugate (G-actin, ThermoFisher Scientific, Cat# D12371) and DAPI (ThermoFisher Scientific, Cat#D1306) for 2 h at room temperature. Cells were then washed thrice in 1×PBS and mounted with FluorSave™ (Merck, Cat#345789) for imaging (Nikon, Eclipse Ti2; Zeiss, Axio Observer Z1 and Nikon, Eclipse TE2000-E). The same exposure settings were used to acquire images from WT and FEZ1-null groups. Images were analyzed with ImageJ/Fiji with quantification details in the following section. At least three independent experiments were performed.

Quantification of IF images

For quantification of F-actin and G-actin (Figure 5E), ImageJ/Fiji was used to obtain fluorescent intensities using the raw integrated density (RawIntDen) measurement under Analyze for both F- and G-actin channels. The G- to F-actin ratios for WT or FEZ1-null hCOs were normalized to the mean WT G- to F-actin ratio for each batch. At least 10 images were acquired from independent fields per group per batch. Data from 3 independent experiments were used to generate the plot.

For quantification of p-VIM and QKI (Figures 6A and 6B), the spots function in Imaris 9.5.1 was used with estimated diameter of nuclei at 6 μm and intensity mean channel of p-VIM$^+$ or QKI$^+$ to filter and generate p-VIM$^+$ or QKI$^+$ spots, which could reflect the corresponding p-VIM$^+$ or QKI$^+$ cells for counting. Total cell numbers were obtained by counting DAPI$^+$ cells using spots function. The localization and number of p-VIM$^+$ or QKI$^+$ cells were grouped as either adjacent to the VZ-like, SVZ-PP-like or SVZ-like zones. The ratios of p-VIM$^+$ or QKI$^+$ cells relative to total cell numbers were calculated by the number of p-VIM$^+$ or QKI$^+$ cells divided by the total cell number in each image. At least 5 different regions were analyzed within one organoid. A total of 8 hCOs from 3 independent experiments were used to perform the quantification for each genotype.

For analyses of EdU, Ki67, and the neuronal layers (Figures 7 and S9), rosette layers were defined as follows.[31,33,54,102] Dense PAX6$^+$ region was identified as VZ-like zone, while the DCX$^+$ or TUJ1$^+$ region that was distant from VZ-like zone was labelled as SVZ-like zone. TBR2$^+$ cell region in WT was chosen as SVZ-like zone while the region widths were used to define the SVZ-like in FEZ1-null genotype. The region outside OSVZ, where cells showed CTIP2$^+$ was determined as PP. Accordingly, each region was manually drawn and the spots function in Imaris 9.5.1 was used to calculate the number of corresponding cells for the respective cell marker in each region and to normalize against total number (DAPI$^+$) of cells (with an estimated diameter of nuclei at 4 μm and intensity mean channel of DAPI$^+$, PAX6$^+$, TBR2$^+$, CTIP2$^+$, EdU$^+$, and Ki67$^+$ to filter, generate and calculate corresponding spots). At least 5 regions were analyzed within each organoid. For layering analyses, a total of 9 hCOs from 4 independent experiments (hESC H1 hCOs) and a total of 6 hCOs from 3 independent experiments (hiPSC hCOs) per genotype were analysed. For EdU and Ki67 quantifications, a total of 6 hCOs were analysed per genotype. VZ-like: ventricular-like zone; SVZ-like: sub-ventricular-like zone; PP-like: preplate-like.

Quantification of cell migration

Migration of GFP+ cells recorded by live imaging was analyzed by the tracking surface over time function in Imaris 9.5.1. In brief, objective with detail of 1.25 μm was used to help identify GFP$^+$ cells. Autoregressive motion with maximum gap size of 3 μm and a distance of 10 μm were used for tracking. Based on these settings, total traceable cell counts were collected in each location. Only cells with more than 7 hours of consecutive migration were used for further analysis. Ectopically migrating cells from rosette were manually screened. Cell track speed, track length and displacement length for each cell were obtained using the Imaris program. The top 10 cells (ranked by absolute value of cell track speed, track length and displacement length, respectively) in each location were chosen and their values were normalized by subtracting the average of last 5 cells (ranked by absolute value of cell track speed, track length and displacement length, respectively) in corresponding

location group to minimize the non-autonomous cell motion. A minimum of 10 different locations from three independent experiments were used to quantify cell migration for each genotype.

QUANTIFICATION AND STATISTICAL ANALYSIS

Statistical analyses were performed on Prism (GraphPad, version 9.2.0) using Student's t-test, one-way ANOVA and two-way ANOVA based on data distribution. The details of the statistical test used for each figure were shown in the corresponding figure captions.